Hydraulic behaviour of the Geul inverted siphon: energy losses, debris accumulation and applicability of a Minimum Energy Loss culvert.

Additional Master Thesis

Dennis Ronckers

TU Delft

Hydraulic behaviour of the Geul inverted siphon:
energy losses, debris accumulation and applicability of a Minimum Energy Loss culvert.

Additional Master Thesis

By

Dennis Ronckers

Submitted to the department of Civil Engineering and Geosciences

Delft University of Technology

December 2022

Supervised by

dr. ir. Davide Wüthrich

dr. ir. Martine Rutten

Personal picture on cover.

TU Delft

Preface

This thesis is written as part of the MSc degree Civil Engineering at the Delft University of Technology, for the specialisation of Hydraulic Engineering.

Being from Limburg myself, it was especially motivating to work on this research. I am glad to have had the opportunity to contribute towards the knowledge of this area and give it some of the attention it deserves and needs. I hope that this report can provide useful insights and perhaps contribute towards improvements someday.

First of all I want to thank my committee members. I would like to thank Davide Wüthrich, my daily supervisor and chairman of the committee, for giving me the freedom to research what I am most interested in and for providing direction when I needed it. I would also like to thank Martine Rutten for helping me find this topic, providing useful feedback and assisting me in establishing some new connections. Besides my committee members I would also like to thank Bas Jonkman for introducing me to this topic, Paul Neering for giving me a tour of the area, and Daan Poppema for some useful discussions on the analysis of debris. Lastly, I would like to thank everyone who sent me pictures or videos of debris at the structure.

Dennis Ronckers
Roermond, December 2022

Abstract

In the area of Bunde in the south of Limburg, the Netherlands, the Geul river flows beneath the Juliana Canal through an inverted siphon before reaching the Meuse. During July 2021 a large scale flood event occurred, showing an insufficient capacity of the inverted siphon when both the Geul and Meuse had high water level.

Such inefficiency can be explained by the significant head losses at the entrance due to a sub-optimal geometry that also favors the accumulation of debris, as proved during the recent flood. Therefore, the purpose of this study is to investigate the hydraulic behavior the Bunde inverted siphon, focusing on potential implementation measures. Two scenarios were considered, the more extreme of which assumes a 1:100 year Geul discharge and a 1:100 year Meuse water level, which is a conservative approximation of the July 2021 conditions. The other scenario assumed a 1:10 year Meuse water level instead.

Initially an analytical model linking discharge and head loss across the structure was developed, which allowed to evaluate the effect of current and alternative inlet designs on the capacity. The model indicated that capacity was strongly dependent on the Meuse water level, proving that the current configuration yielded a barely insufficient capacity for the more extreme scenario. Results showed that this insufficiency could be improved by streamlining the inlet, leading to an increased capacity of up to 14%.

The model also revealed a reduction in flow capacity associated with the debris accumulated at the inlet, for which a detailed inventory was provided based on post-flood images.

Lastly, the study investigated the possibility of replacing the current inverted siphon with a Minimum Energy Loss (MEL) culvert, which differs from regular culverts since it is designed to minimize losses and to have critical flow within the barrel. This allows MEL culverts to perform well for a small head loss; however, since the barrel roof must be lowered X meters to pass under the Juliana Canal, this solution was shown not being feasible for this case.

Overall this study showed that there is potential to increase the hydraulic capacity of the inverted siphon by streamlining the inlet and by keeping it clear of debris. However, more detailed cost-benefit analyses are needed to guarantee optimized flood-protection measures.

Contents

1

Introduction

This chapter gives the motivation and problem statement for this report, as well as a description of the area and the hydraulic structure of interest. Then the research objectives are given and the methodology and report structure are elaborated on.

1.1. Motivation

In July 2021 large parts of Limburg, The Netherlands, were affected by severe floods, as well as parts of Belgium and Germany. One of the main areas that was affected is the municipality of Meerssen, including (but not exclusively) the villages or neighbourhoods of Bunde, Brommelen and Westbroek. An estimation of the flooded area along with water depths is shown in figure 1.1.

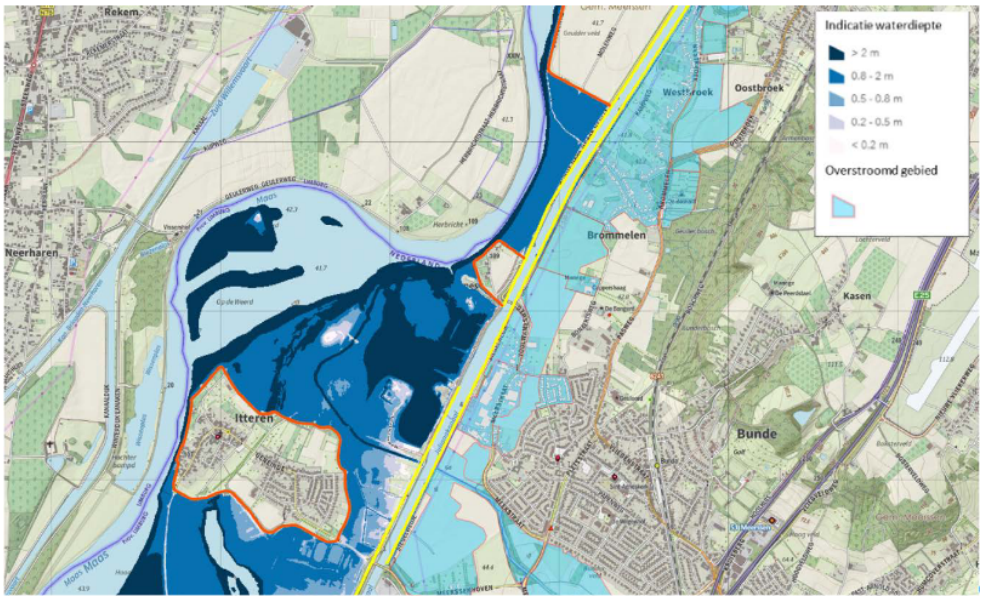

Figure 1.1: Estimation of the flooded area and water depths (ENW, 2021). The shades of dark blue indicate the water depths west of the canal, and the light blue indicates the flooded area east of the canal.

It was estimated that about 1500 houses and 150 company buildings were flooded (Gemeente Meerssen, 2022). While the water depth varied depending on the exact location, several buildings has a meter or more of water inside and as a result many of these houses became uninhabitable for months. As of June 2022, nearly a year later, about 50 families still had not yet been able to return to their homes (Gemeente Meerssen, 2022).

The floods on the east side of the Juliana Canal (light blue area in figure 1.1) were for a large part caused by insufficient capacity of the inverted siphon allowing the Geul to cross the Juliana Canal. However, there was a lot of uncertainty towards the exact capacity of this structure, and towards the further reduction in capacity caused by debris at the structure inlet.

It should be noted that even during events with a more frequent return period the capacity of the inverted siphon could still be insufficient and the surrounding area could still get inundated.

1.2. Area description

In figure 1.2 a simplified overview of the area can be found. The Meuse and the Juliana Canal are prominent elements in this system. The Geul comes from the south-east and passes the village of Bunde before reaching the Juliana Canal, which needs to be crossed to flow into the Meuse on the other side of the canal approximately 2 km further downstream. An inverted siphon under the Juliana Canal makes it possible for the Geul to flow underneath.

About ten meters before the Geul reaches this inverted siphon a seepage stream alongside the canal ends up in the Geul, but this will not be taken into account in this report for reasons explained in appendix B.

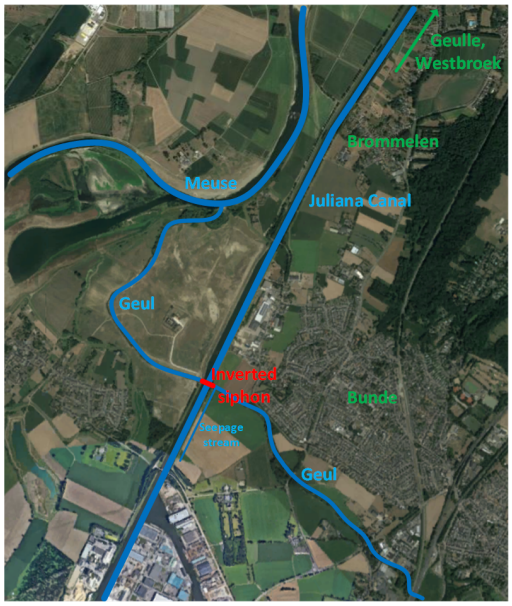

Figure 1.2: Area overview, using aerial view from Google Earth (2022).

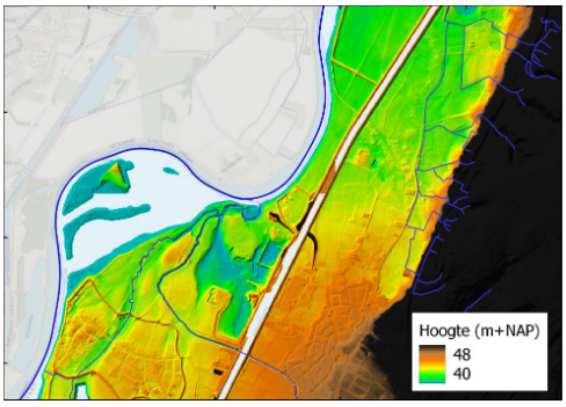

Figure 1.3: Height model based on AHN3 as found in Deltares (2022). Legend indicates height.

1.3. Problem analysis

While floods are usually caused by a combination of several factors in a complex system, it is evident that the floods on the east side of the Juliana Canal were for a large part caused by insufficient capacity of the Geul inverted siphon passing the canal.

It has been estimated that the capacity of this inverted siphon is about 85 m^3/s for normal (low) water levels at the Meuse (Deltares, 2022). However, the water levels at the Meuse were much higher than normal with an estimated return period of roughly 1:100 years, causing the plain between the Meuse and Juliana Canal to flood. This elevated water level on the downstream end of the inverted siphon decreased the capacity of the structure. Additionally, branches and other debris have been observed at the inlet of the inverted siphon (see appendix E) which seem to have blocked the flow to some degree. For these reasons it can be assumed that the actual capacity was less than 85 m^3/s under these circumstances, possibly as low as 50 m^3/s (Deltares, 2022).

Furthermore, it was speculated that the presence of sediment inside the inverted siphon might have additionally decreased its capacity, but research or evidence on this topic is currently lacking.

There is some uncertainty on the actual peak discharge of the Geul during this flood, but estimations range between 85 and 110 m^3/s (Deltares, 2022). Because this estimated discharge is significantly larger than the capacity of the inverted siphon, the Geul flow cannot get to the Meuse on the other side of the Juliana Canal, causing the east side of the canal to flood. An important reason why the flood extended as far as Westbroek, about 4 km north of the structure, is that the land slopes down in this direction as shown in figure 1.3.

1.4. Structure description

As mentioned in section 1.2 the Geul flows underneath the Juliana Canal through an inverted siphon. The inlet of the inverted siphon is shown in figure 1.4. The structure consists of 5 identical barrels that are each 2.50 × 2.50 meter in size (see figure 1.5). First the barrels slope downward under an angle of 11.5° for about 27 meters, followed by a horizontal section of 16 meters, after which they go back up under an angle of 11.5° for about 27 meters again (see figure 1.6). The reason the barrels go down is to pass underneath the Juliana Canal. More technical drawings of the existing structure are given in section A.1.

Figure 1.4: Inlet of the inverted siphon (own picture).

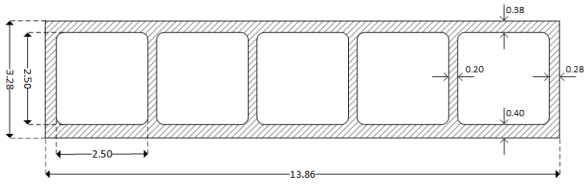

Figure 1.5: Cross section.

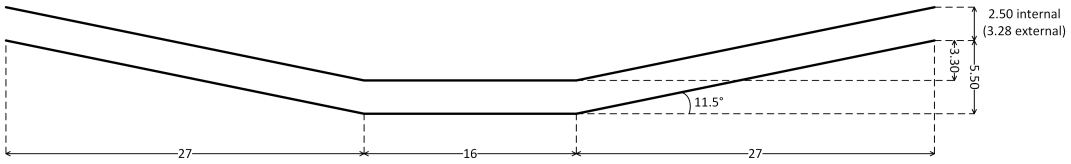

Figure 1.6: Side view.

In figure 1.4 the 1:100 year water level of the Geul is shown, indicated by a depth of 3.83 meter (determined in section 3.2). For this water level only 53% of the flow area can stream straight into the openings, the remaining 47% of the flow area faces a headwall next to or above the openings. From here the water needs to flow around 90° edges to enter the openings. This goes paired with significant head losses. A more streamlined transition from the channel to the inlet could reduce head losses and thus increase the capacity of the structure. This could potentially be a feasible way to increase the capacity of the structure, as the Juliana Canal can remain operational during construction.

Another type of structure that could potentially be used to allow the passage of water underneath the Juliana Canal is a Minimum Energy Loss (MEL) culvert. This is a special type of culvert that is designed for critical flow at every point in the structure to minimise head loss (Chanson, 2007). This means that under design conditions MEL culverts can perform well for small head differences, which would be desirable in situations like July 2021 where the Geul and Meuse both have high water levels simultaneously. MEL culverts will be further explored in section 2.2. This type of design was first explained by McKay (1971), and was further developed by Apelt (1983) for culverts and waterways.

1.5. Objectives

This study has three main objectives:

1. Evaluate the effect of the current and alternative inlet designs on the inverted siphon capacity.
2. Provide a detailed inventory of debris accumulation at the inverted siphon inlet and estimate its effect on the inverted siphon capacity.
3. Explore the possibilities of using a Minimum Energy Loss (MEL) culvert for the Geul crossing the Juliana Canal.

1.6. Methodology

To begin a literature study will be performed. The main focus of this literature study will be on analytical models for inverted siphons including more in-depth research on various head loss factors including head loss due to debris. Subsequently the concepts and design methodology of MEL culverts will be investigated and documented.

In order to reach the first and second research objective an analytical model of the inverted siphon will have to be developed and design conditions will have to be determined. The main design conditions are the Geul discharge and specific energy in the upstream channel section as well as the water level in the Meuse. After the design conditions have been selected the various head loss factors (outlet loss, bend loss and friction loss) at the inverted siphon will be determined.

Next the current and alternative inlet designs will be considered and their corresponding inlet head loss factors will be incorporated into the analytical model. With this, the inverted siphon capacity can be calculated for every type of inlet (for the chosen design conditions). Then an overview of the potential capacity increase for different inlet configurations is given. This completes the first research objective.

For the second research objective visual material of debris accumulated at the structure inlet is gathered by collecting from public sources and requesting photos and videos from local people. Subsequently the debris are categorised by material, size and shape, and the corresponding blockage of the inlet will be determined. Using this blockage a head loss factor for debris can be determined, which is then added to the analytical model to calculate the capacity reduction due to debris. This completes the second research objective.

As part of the third research objective an attempt at designing a MEL culvert for the location of interest is made. The main difficulty (and deviation from literature) in this design will be the obstacle depth prescribed by the Juliana Canal. First a MEL culvert design is made for the actual obstacle depth and design conditions, which is then followed by a sensitivity analysis in which the design discharge and obstacle depth will be varied. This is then followed by a discussion on the feasibility of the MEL culvert design. This completes the third research objective.

1.7. Report structure

The literature study will be documented in chapter 2 of this report. In section 2.1 an analytical model for inverted siphons as well as relevant head loss factors will be explained. Section 2.2 then documents the literature study on MEL culverts.

In chapter 3 the design conditions will be determined: section 3.1 for the design discharge, section 3.2 for the specific energy in the approaching channel and section 3.3 for the downstream water levels.

Chapter 4 applies the analytical model described in section 2.1 to the structure of interest. All parameters and head loss factors are determined here, except for the inlet loss factor and debris loss factor.

In chapter 5 the inlet loss factor is added to the analytical model set up in chapter 4. In section 5.1 the inlet loss factor for the current and alternative inlets is determined. Section 5.2 then shows the effect of the inlet of the inverted siphon capacity, and summarises how much the capacity could potentially be increased for more streamlined inlets.

Debris is covered in chapter 6. Section 6.1 gives an overview of debris that has been observed at the structure inlet. Section 6.2 subsequently determines the debris loss factor for the July 2021 event. Using this debris loss factor section 6.3 will then calculate the corresponding capacity of the structure and compare this to the capacity for a situation without debris.

In chapter 7 the MEL culvert design will be performed and reflected upon. The design procedure is followed in section 7.1 and a summary of the results is given in section 7.2. A sensitivity analysis is performed in section 7.3, which is then followed by a discussion on the design and its feasibility in section 7.4.

Finally chapter 8 will end with conclusions related to the research objectives and reflect on the methods used. Recommendations for the structure of interest will be given, as well as recommendations for further research.

2

Literature study

In this chapter the literature study for this research is documented. Section 2.1 gives theoretical background on analytical models to calculate head loss of inverted siphons. Section 2.2 explains the concepts behind and design of MEL culverts.

2.1. Analytical model for inverted siphons

Al-Juboori & Al-Murshidi (2021) assumed an inverted siphon as shown in figure 2.1. Their model will be used because the structure of interest has the same general shape and fits in this model.

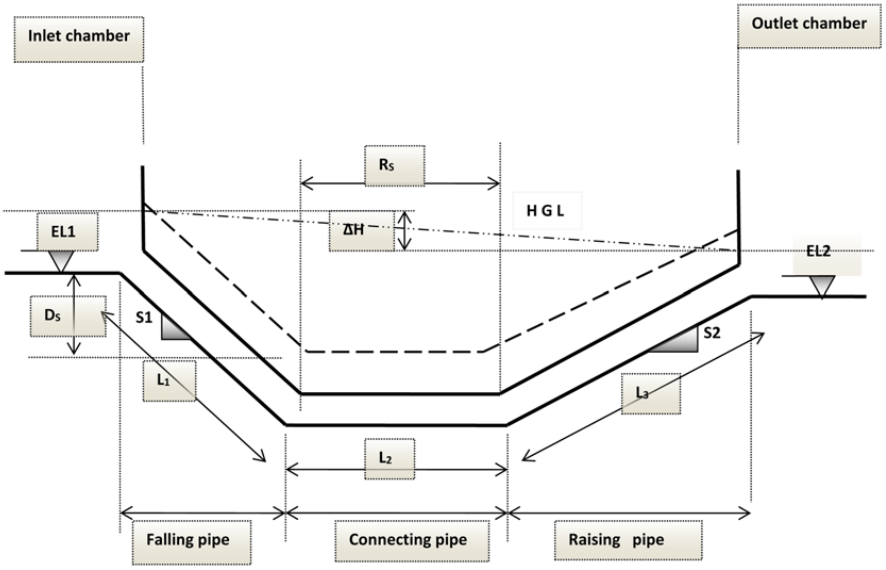

Figure 2.1: Sketch of an inverted siphon (Al-Juboori & Al-Murshidi, 2021)

Subsequently equation 2.1 is given to compute the energy head loss for partially filled pipes.

$$\Delta H = \left(K_{in} + K_{out} + K_s + K_b + \frac{2gn^2 L_t}{R^{\frac{4}{3}}} \right) \frac{u^2}{2g} \tag{2.1}$$

ΔH = total head loss [m]
K_{in} = inlet loss factor [-]
K_{out} = exit loss factor [-]
K_s = screen or debris loss factor [-]
K_b = bend loss factor [-]
n = Manning's roughness coefficient [s/m$^{\frac{1}{3}}$]
L_t = total length of inverted siphon [m]
R = hydraulic radius [m]
u = mean flow velocity through siphon [m/s]

However, for pressurised pipe flow the Darcy-Weisbach equation should be used instead of the Manning equation for wall friction. By replacing the wall friction term in equation 2.1 equation 2.2 can be found:

$$\Delta H = \left(K_{in} + K_{out} + K_s + K_b + f \frac{L_t}{D_h} \right) \frac{u^2}{2g} \tag{2.2}$$

f = Darcy-Weisbach friction coefficient [-]
D_h = equivalent or hydraulic diameter [m]

The determination of the inlet loss factor is presented in chapter 5.

The exit loss factor is often taken as 1.0 without much consideration, but Tullis (2012) found that using the Borda-Carnot expression (equation 2.3) gives much better results for exit loss. This expression deviated at most 6.2% with experimental results for various test set-ups, whereas the simple approach of assuming 1.0 could deviate as much as 187.3%. While these experiments were performed for projecting pipes, it is safe to assume that also for non-projecting outlets equation 2.3 can be used since this is the situation for which the Borda-Carnot equation is derived. Furthermore the tests were performed for low (but non-zero) flow velocities in the downstream channel, similar to the structure of interest.

$$K_{out} = \left(1 - \frac{A_p}{A_{ch}} \right)^2 \tag{2.3}$$

A_p = area of flow in pipe or inverted siphon [m^2]
A_{ch} = area of flow in channel downstream [m^2]

Equation 2.4 for the screen and debris loss factor K_s is given by Meusburger (2002). In this equation p is the blockage factor, which is defined as the area that is blocked by bars or debris divided by the total cross-sectional area. The factor k_F takes into account the shape of the bars or debris, see figure 2.2. Values for each bar shape are provided in table 2.1. The bar shapes a, i, k and l have the same bar shape coefficient, from which it follows that friction losses along the surface of the slide bar are of secondary importance for bars with normal dimensions (Meusburger, 2002).

$$K_s = k_F \cdot \left(\frac{p}{1-p} \right)^{\frac{3}{2}} \tag{2.4}$$

k_F = bar shape factor [-] (table 2.1)
p = blockage factor [-]

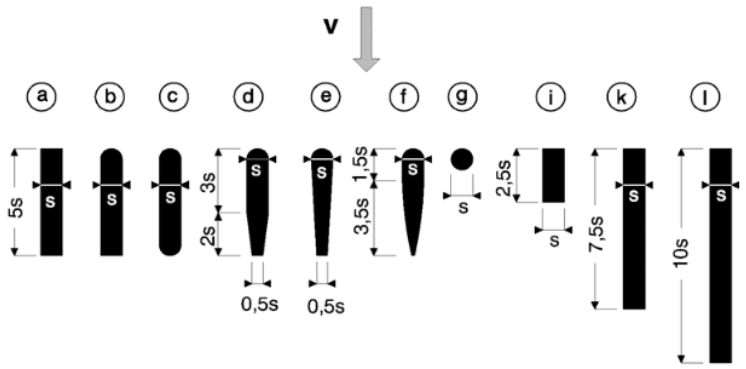

Figure 2.2: Overview of bar shapes as found in Meusburger (2002) after Kirschmer (1926)

Bar shape	a, i, k, l	b	c	d	e	f	g
Shape factor k_F	2.42	1.83	1.67	1.04	0.92	0.76	1.79

Table 2.1: Values for the shape factor k_F, as found in Meusburger (2002) after Kirschmer (1926)

The bend loss factor K_b for vertical bends in inverted siphons is explained by Al-Husseini (2008). He suggest to use formula 2.5 by Weisbach (no source). Al-Juboori & Al-Murshidi (2021) claim that allowances for bend losses only have to be made for bends larger than 20 degrees.

$$K_b = 0.9457 \sin^2\left(\frac{\theta}{2}\right) + 2.047 \sin^4\left(\frac{\theta}{2}\right) \tag{2.5}$$

θ = bend angle [°]

The Darcy-Weisbach friction coefficient f can be determined using the Colebrook-White equation (2.6) which is valid for turbulent flow. This is an implicit equation.

$$\frac{1}{\sqrt{f}} = -2log\left(\frac{k}{3.71 D_h} + \frac{2.51}{Re\sqrt{f}}\right) \tag{2.6}$$

k = wall roughness [m]
D_h = hydraulic diameter [m]
Re = Reynolds number [-]

However, if the Reynolds number and wall roughness k are large (which can be the case for concrete) the second term between brackets can be neglected, meaning that equation 2.6 can be rewritten to equation 2.7 which is explicit.

$$f = \left(\frac{1}{-2log\left(\frac{k}{3.71 D_h}\right)}\right)^2 \tag{2.7}$$

2.2. Minimum Energy Loss (MEL) culverts

Culverts are often used to allow passage of water through an embankment. Typically pipe culverts or box culverts are used. However, they often experience significant energy losses and as a result high elevation of the water head upstream (afflux) for design conditions which can lead to flooding of the surrounding area. Normal culverts are usually designed for critical flow in the barrel, but not at the inlet or outlet.

In contrast with more traditional design, MEL culverts aim to minimise this afflux to reduce flood risk. The two main concepts behind this are (1) streamlining to prevent flow losses and (2) designing for critical flow at every point in the culvert for design conditions (Chanson, 2007). This is done by guiding the channel flow into the barrel through a streamlined inlet, and then expanding the flow back into the natural channel through a streamlined outlet. This is shown in figure 2.3. The concepts behind MEL culverts were first explained by McKay (1971).

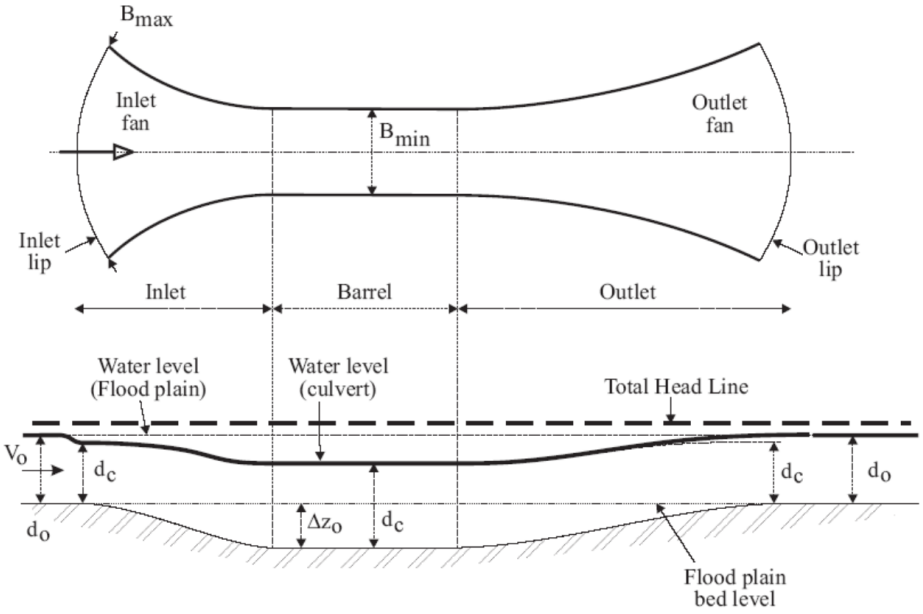

Figure 2.3: Sketch of a Minimum Energy loss culvert operating at design flow with zero afflux (Chanson, 2007)

The maximum width B_{max} is at the inlet and outlet where there is no excavation depth (Δz_0 in figure 2.3). As the excavation depth gets larger the specific energy increases, meaning that the critical depth increases as well so the width can be decreased to B_{min}. Equations 2.8 and 2.9 for B_{max} and B_{min} respectively are given by Chanson (2007). Their derivations are reproduced in section D.2.

$$B_{max} = \frac{Q_{des}}{\sqrt{g \cdot \left(\frac{2}{3} \cdot E_0\right)^3}} \qquad (2.8)$$

$$B_{min} = \frac{Q_{des}}{\sqrt{g \cdot \left(\frac{2}{3} \cdot (E_0 + \Delta z_0)\right)^3}} \qquad (2.9)$$

In which Q_{des} is the design discharge, E_0 is the upstream specific energy and z_0 the excavation depth below the natural channel.

If there is not only an excavation but a lowering of the barrel roof as well, it must be verified that the available depth is at least as large as the critical depth plus a clearing of 20% of the critical depth to allow for undular free-surface flow (Chanson, 2007).

The following design method can be used to develop a hydraulic design for a MEL culvert. It is based on the design procedure by Apelt (1983) as given in Chanson (2004) but this has been modified to account for the presence of an obstacle under which the flow needs to pass underneath, as indicated in figure 2.1 by D_s and R_s. The method described here will be applied to the location of interest in section 7.1.

1. Define the design discharge Q_{des} and the associated initial specific energy E_0 (assuming equilibrium flow in the upstream channel).
2. 2.1 Calculate the inlet and outlet width B_{max} for a rectangular channel, assuming critical flow conditions and natural bed level (i.e. $\Delta z_0 = 0$). B_{max} is measured along the smooth line normal to the streamlines.

   2.2 If obstacle is present: determine the obstacle depth D_s (see figure 2.1) and compute the minimally required excavation depth $\Delta z_{0,req}$ for critical flow.

   2.3 Calculate the barrel dimensions for critical flow. Compute the barrel width B_{min} for a given excavation depth Δz_0 (neglecting energy losses).
   Alternatively: compute the required excavation depth Δz_0 for a given barrel width B_{min}.
3. Define the excavation depth at every point in the inlet and outlet (see figure 2.3), and calculate the corresponding with B at every position to satisfy critical flow.
4. Take into account the energy losses for the chosen design. These are primarily friction loss and form loss. Compare the energy losses to the total head loss available.
5. Check the 'off-design' performances: i.e. $Q > Q_{des}$ and $Q < Q_{des}$.

3

Design conditions

In this chapter the design discharge (section 3.1), the corresponding specific energy upstream of the structure (section 3.2) and the downstream design conditions (section 3.3) are determined.

3.1. Design discharge

The design discharge for the inverted siphon will be taken as the discharge with a return period of 1:100 years. This means that the capacity of the inverted siphon should correspond with the local Geul discharge that has a return period of 1:100 years.

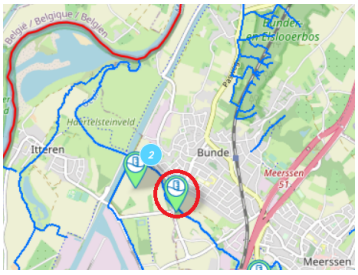

Figure 3.1: Measurement station Maastrichterlaan (Waterschap Limburg, 2022).

While design discharges at this location are difficult to predict accurately, the peak discharge at the Maastrichterlaan measuring station (approximately 900 meter upstream of the inverted siphon) in July 2021 has been estimated between 85 and 110 m^3/s (Deltares, 2022).

Furthermore, the measured water level at this station is only 10 cm lower than the 1:100 year design water level (ENW, 2021, appendix B.2.1), yet several kilometers upstream the measured water levels were up to half a meter higher than the 1:100 year design water level, so it will be assumed that the return period of the July 2021 event was more extreme than 1:100 years. For this reason the design discharge corresponding to a 1:100 year event is taken at the lower end of discharge estimations for July 2021 at:

$$Q_{des} = 85\ [m^3/s]$$

3.2. Initial specific energy

Next, the specific energy just upstream of the culvert E_0 needs to be determined. This follows from the general Bernoulli equation (3.1).

$$E_0 = d + \frac{u^2}{2g} = d + \frac{Q_{des}^2}{2gA^2} \tag{3.1}$$

For a trapezoidal channel, the cross section A is equal to $(b+md)d$ in which b is the bottom width, m the side slope and d the water depth in the middle of the channel. The Bernoulli equation can then be expressed as equation 3.2.

$$E_0 = d + \frac{Q_{des}^2}{2g\left((b+md)d\right)^2} \tag{3.2}$$

From the channel geometry of the Geul follows that b equals 3 m and the side slope is 1:2 (so m equals 2), see figure A.3.

$$b = 3\ [m]$$

$$m = 2\ [-]$$

The corresponding design water level can be derived from the Strickler equation in which k is the Strickler coefficient, S_0 is the bed slope and A and P are the cross-sectional area of the flow and wet perimeter respectively.

$$Q = \frac{kA^{\frac{5}{3}}\sqrt{S_0}}{P^{\frac{2}{3}}} \tag{3.3}$$

$$A = (b + md)d$$
$$P = b + 2d\sqrt{1 + m^2}$$

Since the Geul at this location can be considered a natural channel with short grass, the nondimensional Strickler coefficient k is estimated to have a value of 30 (TU Delft, 2022).

$$k = 30\ [m^{\frac{1}{3}}/s]$$

The bed slope of the Geul is mostly constant over the Dutch reach at 1.87 m/km (Paarlberg, 1990).

$$S_0 = 0.00187\ [-]$$

Solving equation 3.3 iteratively gives a water depth d_{des} of 3.83 m in the middle of the channel. When considering the available depth of 3.95 m (see figure A.3), a freeboard of 3.95 - 3.83 = 0.12 m seems reasonable for design conditions.

$$d_{des} = 3.83\ [m]$$

The initial specific energy can now be calculated by filling in equation 3.2:

$$E_0 = d + \frac{Q_{des}^2}{2g\left((b + md)d\right)^2} = 3.83 + \frac{85^2}{2g((3 + 2 \cdot 3.83) \cdot 3.83)^2} = 4.05\ [m]$$

To verify the design depth d_{des} a comparison with figure 3.2 can be made. There it can be found that the 1:100 year water level upstream of the structure is approximately 44.60 m + NAP. The bed level of 40.75 m + NAP plus the design depth d_{des} is 44.58 m + NAP. This means that the computed design water level is only 2 cm lower than what follows from figure 3.2, so it can be concluded that the computations are correct.

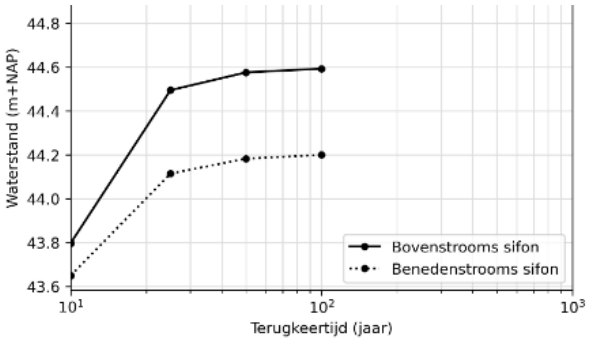

Figure 3.2: Water levels at different return periods at the inverted siphon as found in (Deltares, 2022). Return periods can be found on the horizontal axis, water levels on the vertical axis. The solid line is upstream of the structure, the dotted line is for downstream. Bed level is at 40.75 m + NAP. Note that statistics as of 2014 were used, meaning that the July 2021 event is not included here.

3.3. Downstream conditions

To assess the capacity of the structure a combination of both upstream and downstream water level is required. While the upstream water depth is mostly dependent on the Geul discharge, the downstream depth is mostly dependent on the water levels in the Meuse, since the Geul connects to the Meuse only 2 km further downstream.

As of present there is a lot of uncertainty towards the correlation between extreme events of the Geul and Meuse. For this reason two scenarios will be considered. The first scenario is a Geul discharge with a return period of 1:100 years (as already elaborated in sections 3.1 and 3.2), combined with a downstream water level of return period 1:10 years. The second scenario is again a Geul discharge with a return period of 1:100 years, but combined with a downstream water level of return period 1:100 years.

While it would be beneficial to perform a more fundamental analysis towards the correlation between extreme events of the Geul and Meuse, these two scenarios are believed to be representative of the governing flow regimes that can occur at the inverted siphon.

Scenario 1

Scenario 1 corresponds to the 1:10 year downstream water level. From figure 3.2 follows that this water level equals to 43.65 m + NAP. The downstream bed level is at 40.60 m + NAP, resulting in a tailwater depth d_{tw} of 3.05 m.

$$d_{tw,1} = 3.05\ [m]$$

The available head difference ΔH can then be calculated taking the upstream water level (bed level plus water depth) minus the downstream water level and becomes 0.93 m.

$$\Delta_{H,1} = (40.75 + 3.83) - (40.60 + 3.05) = 0.93\ [m]$$

Scenario 2

Scenario 2 corresponds to the 1:100 year downstream water level. From figure 3.2 follows that this water level equals to 44.20 m + NAP. The downstream bed level is at 40.60 m + NAP, resulting in a tailwater depth d_{tw} of 3.60 m.

$$d_{tw,2} = 3.60\ [m]$$

The available head difference ΔH can then be calculated taking the upstream water level (bed level plus water depth) minus the downstream water level and becomes 0.38 m.

$$\Delta_{H,2} = (40.75 + 3.83) - (40.60 + 3.60) = 0.38\ [m]$$

Flow pattern

In section 2.1 two equations for the head loss of an inverted siphon are given, equation 2.1 for partially filled pipes and equation 2.2 for pressurised flow. Both of these equations assume outlet control conditions.

For both scenario 1 and scenario 2 it holds that $E_0 > 1.2D$ and $d_{tw} > D$ (with D being the barrel height) so according to the classification in appendix C there will be an outlet controlled flow pattern with pressurised flow in the barrel. This is further supported by the fact that inverted siphons are more likely to experience pressurised flow that regular culverts because the barrel is lowered, making a pressure build-up more likely.

The conclusion is that equation 2.2 is most suitable and valid to calculate the head loss over the inverted siphon for both scenario 1 and scenario 2.

4

Analytical model

In this chapter all parameters for the analytical model to compute head loss of the inverted siphon are determined. At the end of the chapter a summary of the results is given.

4.1. Determination of parameters

Method

To compute the inverted siphon capacity for a given available head loss, all parameters in the formula below (equation 2.2) need to be determined first. See section 2.1 for the theoretical background used here.

$$\Delta H = \left(K_{in} + K_{out} + K_s + K_b + f \frac{L_t}{D_h} \right) \frac{u^2}{2g}$$

Flow velocity

The flow velocity u depends on the discharge Q through the inverted siphon. The flow area is the sum of five barrels with a width and height of D. Because the discharge will be the final result of the implicit equation the expression for u below cannot be further simplified.

$$u = \frac{Q}{A} = \frac{Q}{5 \cdot D^2}$$

Hydraulic radius, roughness and total length

The hydraulic radius R_h is equal to the cross-sectional area of the flow A divided by the wet perimeter P. For pressurised flow the entire barrel is filled with water, so each of the five pipes in the barrel has both a height and width of D. Note that the number of pipes drops out of the equation and has no effect on R.

$$R_h = \frac{A}{P} = \frac{5 \cdot D^2}{5 \cdot 4D} = \frac{D}{4} = \frac{2.5}{4} = 0.625 \, [m]$$

Note that the equation above shows that the hydraulic diameter D_h is equal to D of one pipe. This is because the hydraulic diameter D_h is per definition four times the hydraulic radius R_h.

$$D_h = D$$

The Darcy-Weisbach friction coefficient f is largely determined by the Reynolds number and the wall roughness k. These are determined first, so that it can be decided whether the explicit equation 2.7 is sufficiently accurate or if the implicit equation 2.6 can be used.

The flow velocity term in the Reynolds number equation will be substituted by the expression given earlier in this chapter. D_h is the hydraulic diameter, which is four times the hydraulic radius R.

$$Re = \frac{uD_h}{\nu} = \frac{QD}{5 \cdot D^2 \cdot \nu} = \frac{Q}{5 \cdot D \cdot \nu}$$

The kinematic viscosity ν is 10^{-6} m^2/s for water.

$$\nu = 10^{-6}\ [m^2/s]$$

The entire barrel is made of concrete, which is commonly estimated to have a roughness k of 0.3-3 mm. Because no information on the surface texture of the concrete inside the structure is available, an estimation of 2 mm is made.

$$k = 0.002\ [m]$$

Now the Darcy-Weisbach friction coefficient f can be calculated implicitly using equation 2.6 or explicitly using equation 2.7. Assuming a discharge of 85 m^3/s the results from equation 2.6 and equation 2.7 are only off by 0.3%, meaning that the explicit form is sufficiently accurate.

$$f = \left(\frac{1}{-2log\left(\frac{k}{3.71D_h}\right)}\right)^2 = \left(\frac{1}{-2log\left(\frac{0.002}{3.71\cdot 2.5}\right)}\right)^2 = 0.0186\ [-]$$

The total length L_t over which wall friction works is the sum of lengths of the falling pipe L_1, connecting pipe L_2 and rising pipe L_3. This means that for the falling and rising pipe the diagonal distance should be considered. Because the structure is symmetrical, L_1 and L_3 are equal.

$$L_1 = L_3 = 27 \cdot tan(11.5°) = 27.55\ [m]$$

$$L_t = L_1 + L_2 + L_3 = 27.55 + 16 + 27.55 = 71.10\ [m]$$

Exit loss factor

As described in section 2.1 the exit loss coefficient is best described using equation 2.3 which is a function of the area of flow in the inverted siphon A_p and the area of flow in the channel downstream A_{ch}. A_p is the sum of five full pipes with area D^2 each. The outlet is shown in figure 4.1.

Figure 4.1: Outlet of the inverted siphon

$$A_p = 5 \cdot D^2 = 5 \cdot 2.5^2 = 31.25\ [m^2]$$

For the downstream channel the same geometry as the upstream channel is assumed, see figure A.5. Note however that for the exit loss coefficient the cross section immediately downstream of the structure has to be used, which is different from the channel parameters used in section 3.2. Here b is equal to 13.30 m and the side slope m is equal to 1. As explained in section 2.1 this method is valid for relatively low flow velocities downstream, which is the case here.

Scenario 1:

$$A_{ch,1} = d_{tw,1}(b + m \cdot d_{tw,1}) = 3.05 \cdot (13.30 + 1 \cdot 3.05) = 49.87\ [m^2]$$

$$K_{out,1} = \left(1 - \frac{A_p}{A_{ch,1}}\right)^2 = \left(1 - \frac{31.25}{49.87}\right)^2 = 0.1394\ [-]$$

Scenario 2:

$$A_{ch,2} = d_{tw,2}(b + m \cdot d_{tw,2}) = 3.60 \cdot (13.30 + 1 \cdot 3.60) = 60.84\ [m^2]$$

$$K_{out,2} = \left(1 - \frac{A_p}{A_{ch,2}}\right)^2 = \left(1 - \frac{31.25}{60.84}\right)^2 = 0.2365\ [-]$$

Screen or debris loss factor

No debris screens are present, so when debris itself is not considered then K_s is equal to 0.

$$K_s = 0$$

In chapter 6 an analysis of debris will be performed and values of K_s will be determined accordingly.

Bend loss factor

In the inverted siphon two identical bends of 11° are present. The bend loss factor K_b is therefore two times the bend loss factor per identical bend K_b'.

$$K_b = 2K_b'$$

Using equation 2.5 as proposed by Al-Husseini (2008) gives:

$$K_b' = 0.9457\sin^2\left(\frac{\theta}{2}\right) + 2.047\sin^4\left(\frac{\theta}{2}\right) = 0.9457\sin^2\left(\frac{11°}{2}\right) + 2.047\sin^4\left(\frac{11°}{2}\right) = 0.0089\ [-]$$

The bend loss factor would then be $K_b = 0.0177$. This value is small compared to all other loss factors, including the inlet loss factor and debris loss factor determined later in this report. Moreover, it should be noted that Al-Husseini (2008) gave no validity range for the equation above, meaning that it is possible that the equation was derived for larger bends. Since the bends are less than 20 degrees each no allowance for bend loss needs to be made according to Al-Juboori & Al-Murshidi (2021). For these reasons bend loss is assumed to be negligible.

$$K_b = 0\ [-]$$

4.2. Summary and discussion

The resulting values are summarised in table 4.1. Note that K_{in} and K_s have not been determined yet, they are covered in chapter 5 and chapter 6 respectively.

$$\Delta H = \left(K_{in} + K_{out} + K_s + K_b + f\frac{L_t}{D_h}\right)\frac{u^2}{2g}$$

	ΔH [m]	K_{out}	K_b	$f \cdot \frac{L_t}{D_h}$	u [m/s]
Scenario 1	0.93	0.1349	0	0.529	$\frac{Q\ [m^3/s]}{31.25\ [m^2]}$
Scenario 2	0.38	0.2365			

Table 4.1: Summary of parameters

A few assumptions regarding the values in table 4.1 should be highlighted. First of all, for a more accurate representation of the wall friction the roughness of the concrete inside the barrel should be measured, since this is shown to have a significant effect on the friction coefficient. Second, the downstream water level was assumed to be equal to the Meuse water level. This is expected to be a valid assumption because the distance between the inverted siphon and the Meuse is less than 2 kilometers, but it has not been verified. Third, the values of the available head loss ΔH are slightly conservative because the available freeboard of 0.12 meter in the upstream channel was not included.

5

Effect of inlet design

This chapter focuses on the first research objective. In section 5.1 the inlet loss factor K_{in} is determined for the current and alternative inlet configurations. Section 5.2 will shows the effect of the inlet on the structure capacity, and by how much the capacity could potentially be increased for some more streamlined inlets.

5.1. Inlet loss factor

Method

The inlet loss factor K_{in} was defined as $\Delta H_{in} = K_{in} \cdot \frac{u^2}{2g}$ in section 2.1. The goal section 5.1 is to determine K_{in} as a function of the upstream water depth d. There are two contributions to this loss factor: head loss due to a horizontal contraction $K_{in,side}$ and head loss due to a vertical contraction $K_{in,top}$.

$$K_{in} = K_{in,side} + K_{in,top}$$

Figure 5.1 illustrates how the inlet causes head loss at the sides (figure 5.1a) and at the top (figure 5.1b). It clearly shows how the dashed ideal streamlines are blocked by the black structure boundaries.

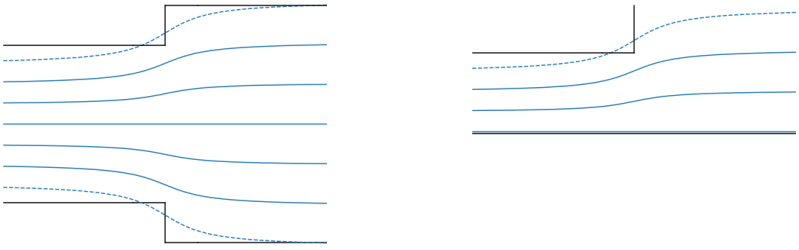

(a) Horizontal contraction causing $K_{in,side}$ (top view)

(b) Vertical contraction causing $K_{in,top}$ (side view)

Figure 5.1: Sketches illustrating inlet loss. Black lines are boundaries provided by the structure inlet, blue lines are ideal flowlines.

Figure 5.2 shows which areas contribute towards each component of the inlet loss. The yellow areas contribute towards $K_{in,side}$, the orange area contributes towards $K_{in,top}$ and the red areas contribute to both. Note that the effect of the four dividing walls between the barrels was neglected.

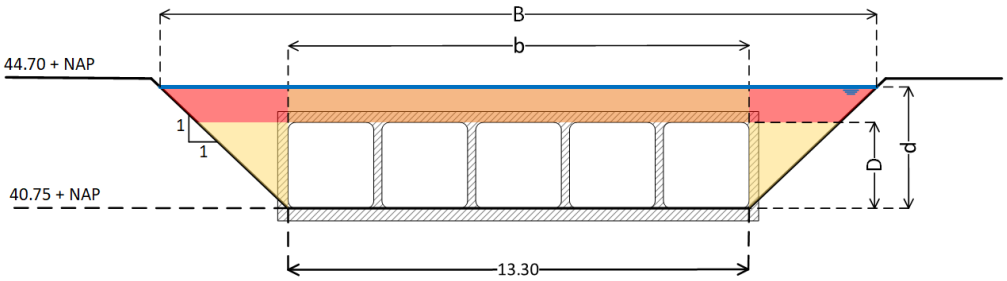

Figure 5.2: Sketch of inlet losses. Cross section shown is immediately upstream of the inlet. Yellow area contributes to side loss, orange to top loss and red to both.

Theory

Yaziji (1968) measured the head loss for several types of horizontal contractions under free-surface flow. These types of contractions are shown in figure 5.3. They are numbered by efficiency, with the lowest number having the least associated head loss.

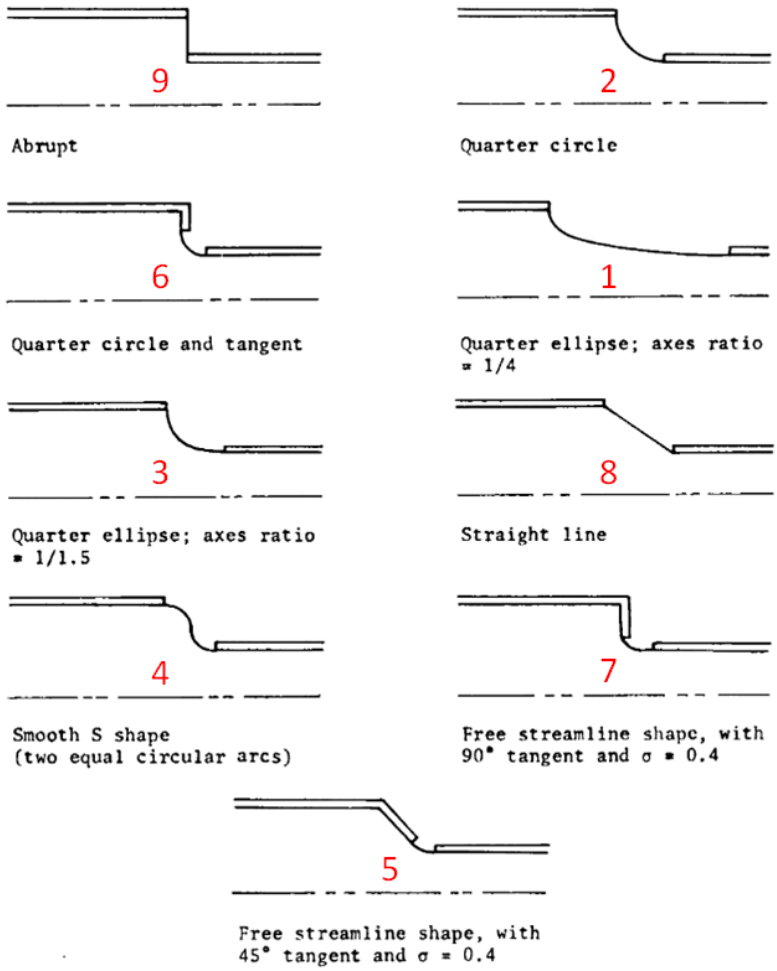

Figure 5.3: Horizontal contractions tested by Yaziji (1968)

All of these configurations were tested for a width ratio b/B (defined as width downstream of contraction / width upstream of contraction) of 1/2, and five of these also for a width ratio of 1/9. The results are summarised in table 5.1.

$\frac{b}{B}$ / Inlet config.	1	2	3	4	5	6	7	8	9
1/2	0.04	0.08	0.085	0.09	0.10	0.11	0.18	0.19	0.41
1/9	-	0.36	-	0.29	-	0.41	0.42	-	0.74

Table 5.1: Inlet loss factors as measured by Yaziji (1968)

The results in table 5.1 were plotted in figure 5.4. An additional constraint was added that for a width ratio of 1 the loss coefficient is 0, since there is no loss when there is no contraction.

All five configurations tested for both the width ratios of 1/2 and 1/9 have been fitted with a first or second order approximation. The abrupt transition matched well with a first order approximation, while the other transitions matched better with a second order approximation.

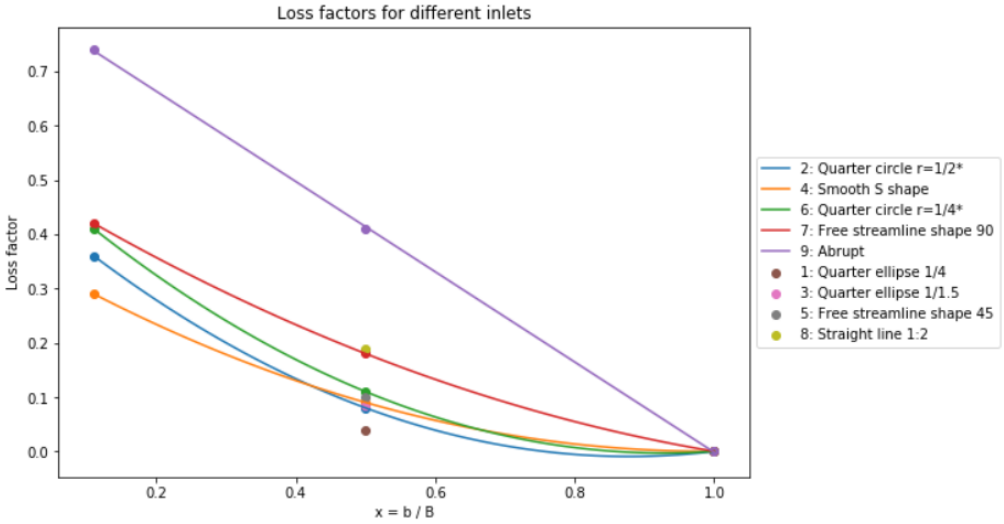

Figure 5.4: Side loss values for different horizontal contractions and width ratios. The dots are measurements by Yaziji (1968). The first and second order approximations have been added as part of this report.

The exact parameters of these fits, defined as in equation 5.1, are summarised in table 5.2.

$$K = a \cdot x^2 + p \cdot x + c \tag{5.1}$$

Inlet configuration	2	4	6	7	9
a	0.6782	0.4252	0.6684	0.2869	0
p	-1.1573	-0.7979	-1.2026	-0.7904	-0.8309
c	0.4791	0.3726	0.5342	0.5053	0.8293

Table 5.2: Fitted parameters for equation 5.1 with $x = \frac{b}{B}$ for side loss or $x = \frac{D}{2 \cdot d - D}$ for top loss

Side loss

For the side loss, the width ratio x_{width} is simply defined as b/B. However, it would be more convenient to express this as a function of the upstream water depth d instead, like equation 5.2. In this equation m is the side slope which is equal to 1 at the inlet (see figure 5.2). $x_{width,des}$ is the width ratio at the water surface.

$$x_{width} = \frac{b}{B} = \frac{b}{b + m \cdot d \cdot 2} \tag{5.2}$$

$$x_{width,des} = \frac{b}{b + m \cdot d_{des} \cdot 2} = \frac{13.30}{13.30 + 1 \cdot 3.83 \cdot 2} = 0.635\ [-]$$

Since the width ratio b/B changes over the depth the side loss factor $K_{in,side}$ should be computed using equation 5.3. The integral boundaries are $x_{width,des}$ for the water surface and 1 for the river bed where the channel width is equal to the inlet width.

$$K_{in,side} = \frac{\int_{x_{width,des}}^{1} K(x_{width})\, dx_{width}}{1 - x_{width}} \tag{5.3}$$

Only configuration 9, the abrupt transition, is relevant for the side loss factor. This is because configuration 9 is currently present at the location of interest. There is no reason to implement any of the other horizontal contractions since the approaching channel is narrower than the inverted siphon inlet. A more efficient inlet configuration will be proposed in section 5.2.

$$K_{in,side,abrupt} = 0.150\ [-]$$

Top loss

The top loss can be computed in a similar manner as the side loss. Instead of the width ratio x_{width} now a height ratio x_{height} should be used. This is defined as the height after the contraction divided by the height before the contraction, pretending that the contraction is symmetrical. In other words, pretending that the extra height above the inlet is also present below the inlet. This gives equation 5.4. Further elaboration can be found in section D.3.

$$x_{height} = \frac{D}{2 \cdot d - D} \tag{5.4}$$

$$x_{height,des} = \frac{D}{2 \cdot d_{des} - D} = \frac{2.50}{2 \cdot 3.83 - 2.50} = 0.484\ [-]$$

There is only a vertical contraction when the water level becomes higher than the inverted siphon inlet, i.e. when $d > D$. Because of this equation 5.5 for $K_{in,top}$ is conditional.

Because the vertical contraction is constant over the width, $K_{in,top}$ has a constant value and does not need to be computed with an integral unlike $K_{in,top}$. The factor 1/2 in equation 5.5 is to take into account that there is only a vertical contraction from the top and not from the bottom.

$$K_{in,top} = \begin{cases} \frac{1}{2} \cdot K(x_{height}), & \text{if } d > D \\ 0, & \text{otherwise} \end{cases} \tag{5.5}$$

The resulting values for $K_{in,side}$, $K_{in,top}$ and K_{in} for each type of top transition are summarised in table 5.3.

Top configuration	2	4	6	7	9
Loss coefficient $K_{in,side}$	0.150				
Loss coefficient $K_{in,top}$	0.022	0.024	0.030	0.047	0.107
Loss coefficient K_{in}	0.172	0.174	0.180	0.197	0.257

Table 5.3: Inlet loss factor values

5.2. Effect of inlet on capacity

Specific energy loss

To determine the relative effect of the inlet configuration on the total energy loss over the inverted siphon, it is more useful to consider the specific energy loss than the head loss. This is because even in a natural channel under uniform flow there will be head loss, but no loss in specific energy. Combining the two expression below with equation 2.2 and leaving out the debris loss factor gives equation 5.6.

$$\Delta E = \Delta H - \Delta z \qquad \Delta z = K_{f,nat} \cdot \frac{u^2}{2g}$$

$$\Delta E = \Delta H - \Delta z = \left(K_{in} + K_{out} + K_b + \left(f \frac{L_t}{D_h} - K_{f,nat} \right) \right) \frac{u^2}{2g} \tag{5.6}$$

Warped horizontal transition

A warped canal transition is also considered to estimate how much the capacity of the inverted siphon could potentially be increased through a reduction of inlet loss. The purpose of this is to have a smooth transition from the trapezoidal cross-section in the canal to a rectangular cross section at the inverted siphon, for which side loss can be neglected ($K_{in,side} = 0$). See figure 5.5 for a schematic, or figure A.6 for a top view.

The optimal design for such a warped transition is outside of the scope for this report. However, according to Hinds (1928): "the length of the transition is determined so that a straight line joining the flow line at the two ends of the transition will make an angle of about 12.5° with the axis of the structure".

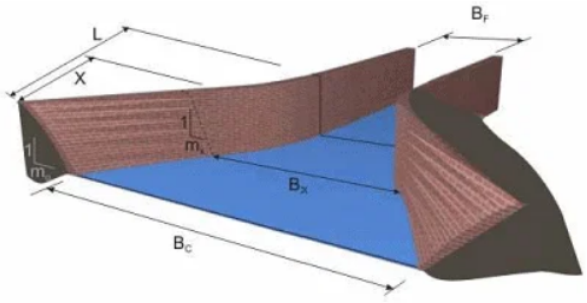

Figure 5.5: Schematic of a warped canal transition (EduRev, 2022)

Capacity for different inlets

Using equation 5.7, table 4.1 and table 5.3 the capacity for different inlet designs can now be calculated. Recall that scenario 1 and scenario 2 were defined in section 3.3.

$$\Delta H = \left(K_{in} + K_{out} + K_b + f\frac{L_t}{D_h}\right)\frac{u^2}{2g} \tag{5.7}$$

Scenario 1

Table 5.4 summarises the capacity of the inverted siphon for the five different top configurations, both for the current horizontal contraction and for an optimal warped transition with no side loss.

Top configuration	2	4	6	7	9
Capacity [m^3/s] (current)	146.0	145.8	145.3	143.9	139.1
Capacity [m^3/s] (warped)	161.2	160.9	160.2	158.3	152.0

Table 5.4: Capacity for different inlet configurations (scenario 1).

To determine the relative effect of the inlet on the inverted siphon capacity, the expression for head loss should be converted to an expression for specific energy loss (equation 5.6).

$$\Delta E = \Delta H - \Delta z = \left(K_{in} + K_{out} + K_b + \left(f\frac{L_t}{D_h} - K_{f,nat}\right)\right)\frac{u^2}{2g}$$

$$(0.93 - 0.15) = (0.257 + 0.1349 + 0 + (0.529 - 0.149))\frac{\left(\frac{Q}{31.25}\right)^2}{2g}$$

By considering the K factors above, it can be determined that for scenario 1 the inlet is responsible for 33.3% of the total specific energy loss due to the structure.

Table 5.5 summarises how much the capacity of the structure could potentially be increased for a streamlined horizontal transition, for a streamlined top of the inlet (configuration 2), and for both simultaneously. By implementing both measures, the capacity can be increased by 28.7 m^3/s or 20.4%.

	Capacity increase [m^3/s]	Capacity increase [%]
Streamlining sides	12.9	9.3
Streamlining top	6.9	5.0
Streamlining sides & top	22.1	15.9

Table 5.5: Potential capacity increase for more streamlined inlets (scenario 1).

Scenario 2

Table 5.6 summarises the capacity of the inverted siphon for the five different top configurations, both for the current horizontal contraction and for an optimal warped transition with no side loss.

Top configuration	2	4	6	7	9
Capacity [m^3/s] (current)	88.1	88.0	87.8	87.0	84.4
Capacity [m^3/s] (warped)	96.2	96.0	95.7	94.7	91.4

Table 5.6: Capacity for different inlet configurations (scenario 2).

To determine the relative effect of the inlet on the inverted siphon capacity, the expression for head loss should be converted to an expression for specific energy loss (equation 5.6).

$$\Delta E = \Delta H - \Delta z = \left(K_{in} + K_{out} + K_b + \left(f\frac{L_t}{D_h} - K_{f,nat}\right)\right)\frac{u^2}{2g}$$

$$(0.38 - 0.15) = (0.257 + 0.2365 + 0 + (0.529 - 0.404))\,\frac{\left(\frac{Q}{31.25}\right)^2}{2g}$$

By considering the K factors above, it can be determined that for scenario 2 the inlet is responsible for 41.6% of the total specific energy loss due to the structure.

Table 5.5 summarises how much the capacity of the structure could potentially be increased for a streamlined horizontal transition, for a streamlined top of the inlet (configuration 2), and for both simultaneously. By implementing both measures, the capacity can be increased by 10.2 m^3/s or 12.6%.

	Capacity increase [m^3/s]	Capacity increase [%]
Streamlining sides	7.0	8.3
Streamlining top	3.7	4.4
Streamlining sides & top	11.8	14.0

Table 5.7: Potential capacity increase for more streamlined inlets (scenario 2).

Discussion

Figure 5.6 below shows the capacity of the inverted siphon for a range of downstream water levels, while the upstream water level remains fixed at design water level. The graph starts at a downstream water depth of 2.50 meter which is when the outlets start to be submerged.

Looking at the dashed vertical line for scenario 2 (both Geul and Meuse 1:100 year event) one can see that as the downstream water level increases, the potential capacity increase for streamlined sides, top or both (green, orange and red respectively) compared to the current capacity (blue) decreases. However, the higher downstream water levels are the situations for which a capacity increase would be needed most.

For example, for a 1:10 year water level of the Meuse (scenario 1) the inverted siphon capacity could potentially be increased by 22.1 m^3/s, but even without an increase the capacity of 139.1 m^3/s is already more than sufficient for events even more extreme than July 2021. The potential capacity increase for a 1:100 year water level of the Meuse might be less at only 11.8 m^3/s, but in this scenario the capacity could be increased from 0.6 m^3/s below the 1:100 year Geul discharge to up to 11.2 m^3/s above 1:100 year Geul discharge.

If the downstream water level is 44.18 m + NAP (depth of 3.58 m) then the capacity of the structure is equal to the 1:100 year design discharge of the Geul at 85 m^3/s. According to figure 3.2 this responds to a Meuse water level with a return period of 1:50 years[1].

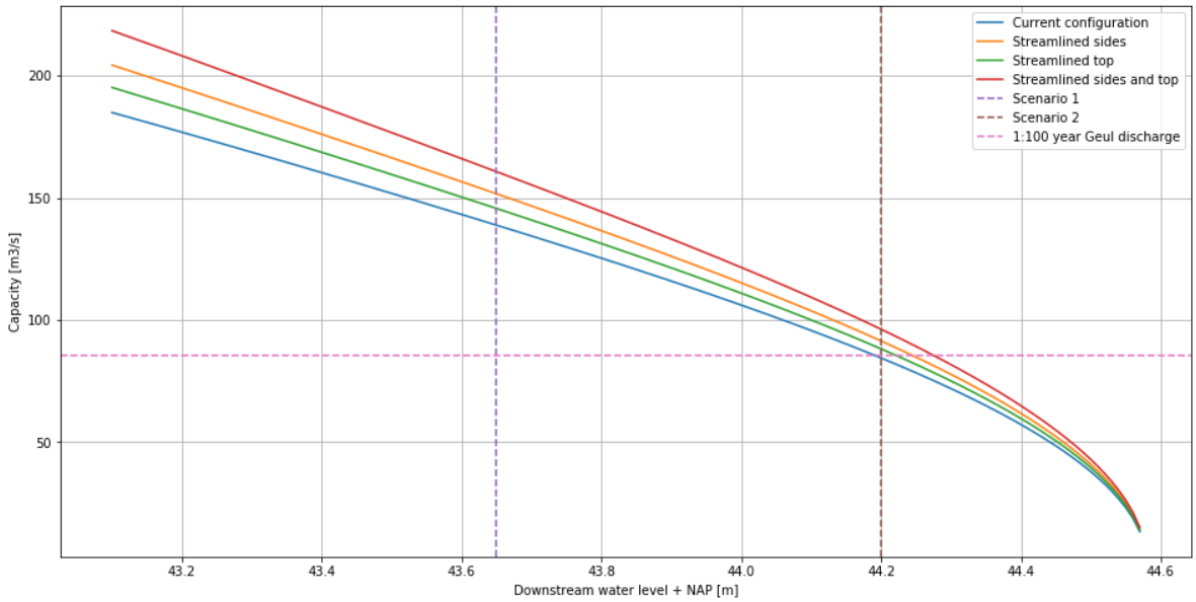

Figure 5.6: Inverted siphons capacity as a function of the downstream water level. Graph starts at a downstream water depth of 2.50 meter which is when the outlets start to be submerged.

Regarding the side loss coefficient, it is important to realise that an optimal hydraulic design was assumed, which has no side loss at all. This means that the given capacity increase due to streamlining of the sides is an upper limit, and while a better hydraulic design can approach this upper limit it will be difficult or costly to actually reach this upper limit.

Furthermore the top loss coefficient is only an approximate value because of two reasons. First, the method used was derived for horizontal contractions, but for the downward contraction gravity works favourably. This effect has not been taken into account. Second, the screens above the openings have not been incorporated into the model. Because there is an open space between the raised screens and the headwall of the structure this was too difficult to calculate analytically.

[1]The 1:50 and 1:100 year Meuse water level are only off by about 2 centimeters. This is why in figure 5.6 it seems as if the capacity (blue line) intersects with the 1:100 year Geul discharge at a 1:100 year Meuse water level. In reality this is at a 1:50 year Meuse water level.

6

Debris

This chapter analyses the accumulated debris and its effect on the inverted siphon. Section 6.1 aims to give an impression of types and dimensions of debris observed. In section 6.2 the debris loss factor K_s is determined using July 2021 conditions, and subsequently in section 6.3 the effect of debris on the capacity of the inverted siphon is calculated. Section 6.4 offers a brief discussion. Additional photographic material is provided in appendix E.

6.1. Overview of debris

Methodology

This chapter aims to summarise the types and dimensions of debris (deposits) that have been observed at the inverted siphon inlet. One of the analysed deposits developed during the flood event in July 2021. Another deposit that was documented developed during a period of high water levels in February 2022.

Dimensions of discernible branches were determined using visual data processing software. First a reference line needs to be drawn along a known distance, such as the width of the openings. Then the software calculates the length of a line along a branch using the same pixel-to-distance ratio as the reference line. To obtain accurate results the reference line and measurement line should be placed at approximately the same 'depth' in the picture, otherwise the assumption of having an equal pixel-to-distance ratio is not valid.

February 2022

The picture in figure 6.1 was taken during February 2022 around the time of a relatively high Geul discharge. While not nearly as extreme as the July 2021 event, a rough estimate shows that the return period of this discharge could have been about 1:10 years. A clear deposit can be observed around the center of the inlet and around the right bank. Although individual branches are not clearly identifiable, and the height (or depth) of the deposit cannot be observed, this picture still gives useful insight into debris accumulation that can occur.

Number	length [m]	diameter [m]	length/diameter ratio [-]
20	7.00	0.20	35.00

Table 6.1: Identification of branches (February 2022)

While this deposit blocks a significant portion of the inlet, the debris seems to be floating. This means that for the design water level (about 1.35 meter above the inlet openings) the main body of the debris is expected to float above the inlet openings.

Figure 6.1: Debris during February 2022 event

July 2021

The table below summarises only the main branches observed in front of the inlet after the July 2021 flood. Note however that branch 23 would not have blocked the inlet at its current position. The other branches provide a blockage of 1.3 m^2, or 4.1%.

Figure 6.2: Debris after July 2021 event (overview)

Number	length [m]	diameter [m]	length/diameter ratio [-]
21	7.43	0.09	82.56
22	5.10	0.04	127.50
23	6.00	0.05	120.00
24	6.88	0.06	114.67

Table 6.2: Identification of branches (July 2021)

Besides branches there also seems to be a piece of agricultural plastic being stuck between some branches, see figure 6.3. This sheet of plastic has a surface area of about 1 m^2, which corresponds to a blockage of 3.2% of the flow area of the inlet. Even though it is hard to say if the plastic was in the same position during the extreme discharge, this will be assumed because it represents the worst-case scenario of the effect of debris on the capacity.

Figure 6.3: Debris after July 2021 event (left) from Deltares (2022)

Furthermore the right two barrel inlets were blocked by bundles of smaller branches with leaves, see figure 6.4. Unlike the main branches identified in table 6.2 these bundles should be modelled with a porosity. The deposit is about about 5.0 meters wide and 1.5 meters high (only including area in front of inlet openings), with an estimated effective porosity of about 60%. This corresponds to a blocked area of 5.0 × 1.5 × (1 - 0.60) = 3.0 m^2, or a blockage of 9.6%.

Figure 6.4: Debris after July 2021 event (right) from Deltares (2022)

Generally observed debris

The picture in figure 6.5 was taken early in 2022, but is not directly related to an extreme event. It shows that a cable in front of the inlet may potentially have been the cause of this accumulation, or at least contributed to it.

Number	length [m]	diameter [m]	length/diameter ratio [-]
1	2.40	0.28	8.57
2	0.89	0.07	12.71
3	1.10	0.05	22.00
4	0.80	0.03	26.67
5	0.72	0.02	36.00
6	0.96	0.02	48.00
7	0.42	0.02	21.00
8	0.75	0.02	37.50
9	0.59	0.03	19.67

Table 6.3: Identification of branches (general, part 1)

Figure 6.5: General debris (1)

Number	length [m]	diameter [m]	length/diameter ratio [-]
10	1.28	0.06	21.33
11	1.21	0.05	24.20
12	0.88	0.09	9.78
13	1.60	0.05	32.00
14	0.79	0.03	26.33
15	0.83	0.04	20.75
16	0.70	0.02	35.00

Table 6.4: Identification of branches (general, part 2)

Figure 6.6: General debris (2)

Branch 17 is one of the largest branches observed in terms of diameter, alongside with branch 1. While such branches were not observed in July 2021, their presence here shows that it is not unlikely to find such branches during a high discharge event.

Number	length [m]	diameter [m]	length/diameter ratio [-]
17	2.80	0.25	11.20
18	1.22	0.04	30.50
19	1.03	0.04	25.75

Table 6.5: Identification of branches (general, part 3)

Figure 6.7: General debris (3)

6.2. Head losses associated with debris accumulation

Method

Recall that the debris loss factor K_s can be calculated using equation 2.4:

$$K_s = k_F \cdot \left(\frac{p}{1-p} \right)^{\frac{3}{2}}$$

k_F = bar shape factor [-]
p = blockage factor [-]

In this section the debris loss factor will be calculated for July 2021 conditions. This decision was made based on two reasons, namely that during the July 2021 event debris provided blockage to the flow to an unknown degree, and because enough visual material is available to make an assessment. The only other event with sufficient visual material is the February 2022 event, but the debris seen here seems to be of floating nature. For design conditions the water level would then be 1.43 meter above the inlet openings, meaning that a significant amount of the debris would float above the inlets and hardly obstruct the flow.

Shape factor

The shape loss factor k_F should be determined using table 2.1 and the corresponding figure 2.2. While this method was originally developed for bars in trash screens there are many similarities with debris in the form of branches, which is the main type of debris observed at the structure of interest.

Looking at figure 2.2 bar shape *g* effectively resembles round and straight branch in vertical position, while bar shapes *c, d, e* and *f* could resemble a branch oriented parallel to flow direction. Out of these shapes bar *c* is assumed to be most representative of the natural branches. This is because while there will be some branches that are more streamlined like shape *d, e* or *f*, others might have some outcroppings or irregularities instead, hence shape *c* is believed to be representative for horizontally oriented branches. Bar shapes *a, i, k* and *l* are too rectangular to resemble natural branches.

The sheet of plastic that was observed is most similar to bar shape *a*. While this is a rather coarse approximation, the limited area blocked by plastic compared to branches makes this sufficiently feasible.

Now, according to table 2.1 $k_{F,c} = 1.67$ and $k_{F,g} = 1.79$. The resulting value for k_F will be somewhere in between $k_{F,c}$ and $k_{F,g}$ for branches, because under natural conditions branches can have any orientation (although most floating branches will have a mostly horizontal orientation). However, to also account for the sheet of plastic $k_F = 1.91$ is chosen as a conservative average[1].

$$k_F = 1.91\ [-]$$

Blockage factor

The total blockage factor is the sum of the blockages due to branches, plastic and bundles as described in section 6.1 in the July 2021 subsection. The large branches contribute towards a blockage of 4.1% of inlet flow area, plastic 3.2% and the deposit consisting of bundles of smaller branches 9.6% when corrected for porosity. The total blockage is then 16.9% of the inlet flow area.

$$p = p_{branches} + p_{plastic} + p_{bundles} = 0.041 + 0.032 + 0.096 = 0.169\ [-]$$

Now the debris loss factor K_s can be calculated using equation 2.4 and the parameters determined in this section.

$$K_s = k_F \cdot \left(\frac{p}{1-p} \right)^{\frac{3}{2}} = 1.91 \cdot \left(\frac{0.169}{1-0.169} \right)^{\frac{3}{2}} = 0.1752\ [-]$$

[1] Determined using $k_{F,a}$ for plastic and $k_{F,g}$ for natural wood, then calculated as a weighted average by blockage factor.

6.3. Effect of debris on capacity

Using equation 6.1, table 4.1, the inlet loss value for the existing inlet configuration determined in section 5.1 and the debris loss factor determined in section 6.2, the capacity of the structure with debris can now be calculated. Scenario 1 and scenario 2 were defined in section 3.3 as a 100 year return period discharge of the Geul combined with a 10 and 100 year return period water level of the Meuse respectively. The specific energy loss equation was derived in section 5.2.

$$\Delta E = \Delta H - \Delta z = \left(K_{in} + K_{out} + K_s + K_b + \left(f \frac{L_t}{D_h} - K_{f,nat} \right) \right) \frac{u^2}{2g} \tag{6.1}$$

Scenario 1

In scenario 1 the capacity of the structure with debris like observed during July 2021 is 127.5 m^3/s, this is 11.6 m^3/s less than for a situation without debris, so the debris causes a capacity reduction of 8.3%.

$$(0.93 - 0.15) = (0.257 + 0.1349 + 0.1752 + 0 + (0.529 - 0.149)) \frac{\left(\frac{Q}{31.25}\right)^2}{2g}$$

By considering the K factors above (equation 6.1 filled in for scenario 1), it can be concluded that for scenario 1 debris is responsible for 18.5% of the total specific energy loss due to the structure.

Scenario 2

In scenario 2 the capacity of the structure with debris like observed during July 2021 is 78.0 m^3/s, this is 6.4 m^3/s less than for a situation without debris, so the debris causes a capacity reduction of 7.6%.

$$(0.38 - 0.15) = (0.257 + 0.2365 + 0.1752 + 0 + (0.529 - 0.404)) \frac{\left(\frac{Q}{31.25}\right)^2}{2g}$$

By considering the K factors above (equation 6.1 filled in for scenario 2), it can be concluded that for scenario 2 debris is responsible for 22.1% of the total specific energy loss due to the structure.

6.4. Discussion

The analysis showed that the debris accumulation in July 2021 and in February 2022 looked very different. In July 2021 the debris consisted mostly of larger branches with leaves and also showed some plastic sheets. In February 2022 there were mostly small branches without leaves that formed a floating deposit. These differences can partially be explained by the fact that the Geul discharge was higher in July 2021 and thus the Geul was able to transport more and larger pieces of debris. Another reason is seasonal variability, during winter conditions small branches are weaker and have less leaves.

Implementation of a debris collection system upstream of the inverted siphon could be beneficial as the structure's capacity is already (barely) insufficient for a 1:100 year Geul discharge and 1:100 year Meuse water level. Presence of debris would further reduce the capacity and increase the scale of flooding and damage during extreme events. Such a system should primarily focus on keeping large branches away from the inverted siphon inlet, as small branches are more likely to pass through the inverted siphon or form a floating deposit.

However, as of present there is little research available on the probability of formation of debris deposits. For this reason no accurate estimation of the true failure probability of the inverted siphon can be made. Further research on this topic is recommended to be able to incorporate capacity reduction due to debris accumulation into safety regulations.

7

Design of a MEL culvert

This chapter is related to the third research objective. The possibilities of a MEL culvert for the Geul at the Juliana Canal is investigated. Section 7.1 performs the design procedure that is explained in section 2.2. In section 7.2 a summary of the design can be found. A sensitivity analysis is performed given in section 7.3. Section 7.4 will reflect on the procedure and discuss practical feasibility of this design.

7.1. Design procedure

Step 1

The first step is to determine the design discharge Q_{des} and initial specific energy at the culvert inlet E_0. These have already been determined in chapter 3, see section 3.1 for Q_{des} and section 3.2 for E_0.

$$Q_{des} = 85\ [m^3/s]$$

$$E_0 = 4.05\ [m]$$

Step 2

Step 2.1: Inlet- and outlet width

Equation 2.8 can be used to calculate the inlet- and outlet width. In principle this comes down to the width of a rectangular cross section that can convey the same discharge as the river section upstream assuming critical flow.

$$B_{max} = \frac{Q_{des}}{\sqrt{g \cdot \left(\frac{2}{3} \cdot E_0\right)^3}} = \frac{85}{\sqrt{g \cdot \left(\frac{2}{3} \cdot 4.05\right)^3}} = 6.12\ [m]$$

The corresponding critical depth for this rectangular cross section is then as follows.

$$d_c = \frac{2}{3} E_0 = 2.70\ [m]$$

Step 2.2: Obstacle depth and required excavation depth

In this situation the Juliana Canal provides an obstacle that the MEL culvert needs to pass underneath. The depth of this obstacle is 3.30 m below the bed level at the culvert inlet, see figure A.1.

$$D_s = 3.30\ [m]$$

To ensure free-surface flow the in the culvert barrel, the water level must be lower than the obstacle level. In other words, the excavation depth minus the local water depth must be larger than the obstacle depth. This can be expressed in the form of equation 7.1 as already given in section 2.2, in which d is increased by 20% to provide clearance for undular flow.

$$\Delta z_{0,req} - 1.2d \geq D_s \tag{7.1}$$

When critical flow is prescribed, d can be replaced by d_c which is equal to two thirds of the initial specific energy plus the increase due to bed level lowering $\frac{2}{3}(E_0 + \Delta z_{0,req})$:

$$\Delta z_{0,req} - 1.2 d_c \geq D_s$$

$$\Delta z_{0,req} - 1.2 \cdot \frac{2}{3}(E_0 + \Delta z_{0,req}) \geq D_s$$

$$\Delta z_{0,req} - \frac{4}{5}(E_0 + \Delta z_{0,req}) \geq D_s$$

$$\frac{1}{5}\Delta z_{0,req} - \frac{4}{5}E_0 \geq D_s$$

The result is equation 7.2.

$$\Delta z_{0,req} \geq 4E_0 + 5D_s \tag{7.2}$$

The final values are then as follows:

$$\Delta z_{0,req} \geq 4 \cdot 4.05 + 5 \cdot 3.30 = 32.70\ [m]$$

$$d_c = \frac{2}{3}(E_0 + \Delta z_{0,req}) = \frac{2}{3}(4.05 + 32.70) = 24.50\ [m]$$

In case the clearance of 20% of the critical depth to account for undular flow is not deemed necessary, equation 7.3 should be used instead of equation 7.2.

$$\Delta z_{0,req} \geq 2E_0 + 3D_s \tag{7.3}$$

Step 2.3: Excavation depth and barrel width
Because the required excavation depth is already large and impractical there is no reason to make the excavation depth even larger than required, therefore:

$$\Delta z_0 = \Delta z_{0,req} = 32.70\ [m]$$

Which means that the corresponding depth in the barrel can be calculated using equation 2.9.

$$B_{min} = \frac{Q_{des}}{\sqrt{g \cdot \left(\frac{2}{3} \cdot (E_0 + \Delta z_0)\right)^3}} = \frac{85}{\sqrt{g \cdot \left(\frac{2}{3} \cdot (4.05 + 32.70)\right)^3}} = 0.22\ [m]$$

Step 3, 4 and 5

Because the results of step 2 already show that the MEL culvert design for this situation is highly unfeasible (explained further in section 7.4) it is not deemed useful to further finish the design procedure.

Step 3 would lead to a very large length of the culvert (much longer than the Juliana Canal width) to allow for a smooth transition between the inlet/outlet and barrel since the culvert has a completely different width and height at these locations.

Step 4 would then likely introduce significant energy losses due to the large variations in shape which would in turn make the design even less feasible.

Subsequently step 5 is expected to show that the culvert does not perform well for off-design conditions due to its unusual shape.

7.2. Design summary

A summary of all results for both the calculations with and without 20% is given is table 7.1.

	B_{max} [m]	$h_{inlet/outlet}$ [m]	B_{min} [m]	h_{barrel} [m]	Δz_0 [m]
With clearance	6.12	3.24	0.22	29.40	32.70
Without clearance	6.12	2.70	0.48	14.70	18.00

Table 7.1: MEL culvert design summary

7.3. Sensitivity analysis

To get a better understanding of the effect of different parameters on the design a brief sensitivity analysis is performed. The governing parameters that are selected are the discharge Q and obstacle depth D_s, since these are the most influential on the design.

The channel properties have some effect on the inlet and outlet shape but hardly influence the barrel shape due to the significant obstacle depth. Because in this situation the barrel shape is governing for the feasibility of the MEL culvert design, the channel properties are not included in this sensitivity analysis.

Figure 7.1 shows the effect of discharge on the excavation depth, corresponding barrel width and height for both the design approach with and without a clearance of 20% of the critical depth. The dotted lines indicate discharges corresponding to a range of return periods.

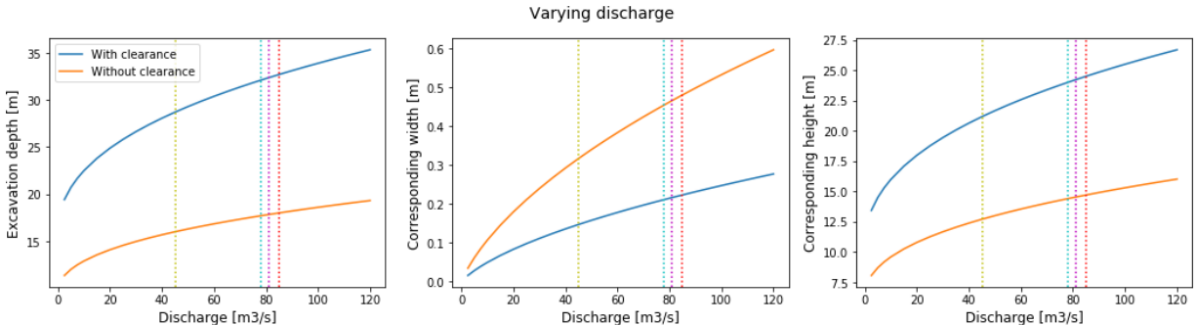

Figure 7.1: Varying discharge. The dotted lines indicate discharges for extreme events with a return period of 10 years (yellow), 25 years (light blue), 50 years (purple) and 100 years (red). Values are based on figure 3.2.

Figure 7.2 shows the effect of obstacle depth on the excavation depth, corresponding width and corresponding height for both the design approach with and without a clearance of 20% of the critical depth. The dashed line indicates the obstacle depth that is present at the location of interest. Recall that the obstacle depth is defined as shown in figure 2.1. The lines start where the obstacle begins to touch the initial water surface.

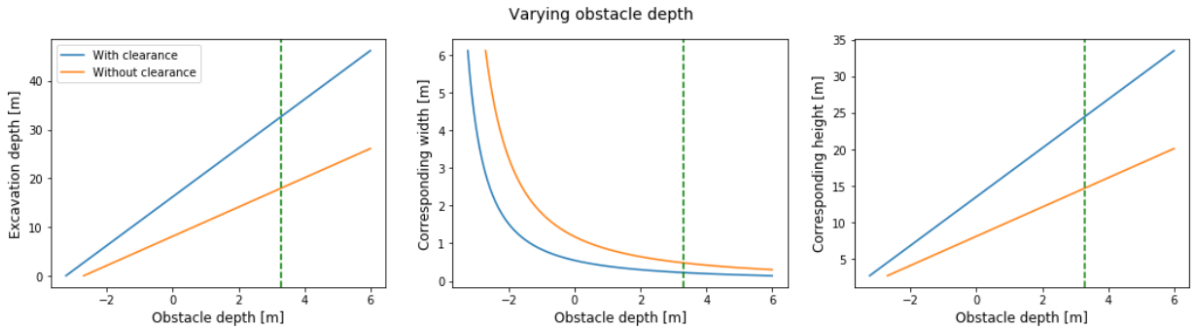

Figure 7.2: Varying obstacle depth D_s (see figure 2.1 for definition). Figure starts at -2.74 m and -2.28 m because any obstacle higher than this will be above the water surface for design discharge. The green dashed line indicates the real obstacle depth in this design.

7.4. Design discussion

The present section investigated the use of a MEL culvert to allow passage of the water in open channel conditions, below the Juliana Canal. Figure 7.2 shows that a MEL culvert becomes unfeasible for increasing obstacle depth D_s, which is the depth of the Juliana Canal below the approaching channel bed level. The required excavation depth increases linearly by 5 D_s for a clearance of 20% (equation 7.2), or by 3 D_s without a clearance of 20% (equation 7.3).

Looking at the middle graph of figure 7.2, it becomes clear that the corresponding width rapidly decreases for increasing obstacle depth. This can be problematic because such a drastic change in the cross-section shape (from 6.12 meter width × 3.24 m height to 0.22 meter width × 29.40 meter height) can lead to significant energy losses (which is against the principle of a MEL culvert) unless the length of the inlet and outlet is significantly increased to smoothen this transition. However, such a transition of at least tens of meters at both the inlet and the outlet will have a major effect on the material and construction costs of the structure.

Furthermore, a cross section of 0.22 meter width × 29.40 meter height in the barrel means that every part of the flow area is within 11 centimeters of a wall, which will generate large amounts of wall friction compared to a more regular cross-section shape, making this design even less feasible.

In addition, it is questionable if a clearance of 20% for undular flow is sufficiently accurate for a depth to width ratio of >100, since this value has likely been derived for more regular depth to width ratios.

The conclusion is that a MEL culvert is not feasible for the location of interest because of the significant obstacle depth prescribed by the Juliana Canal.

8

Conclusions and recommendations

During the July 2021 flood event in the south of the Netherlands the inverted siphon allowing the Geul to cross the Juliana Canal proved to be of insufficient capacity. The capacity was further reduced by debris accumulation at the structure inlet.

Three research objectives for this study were specified to obtain better insights into why the capacity of the inverted siphon was insufficient, as well as to identify potential improvements:

1. Evaluate the effect of the current and alternative inlet designs on the inverted siphon capacity.
2. Provide a detailed inventory of debris accumulation at the inverted siphon inlet and estimate its effect on the inverted siphon capacity.
3. Explore the possibilities of using a Minimum Energy Loss (MEL) culvert for the Geul crossing the Juliana Canal.

In this report two scenarios were analysed, of which the most extreme scenario assumed a 1:100 year Geul discharge of 85 m^3/s in combination with a 1:100 year Meuse water level of 44.20 m + NAP. According to the analytical model that was developed, the capacity of the inverted siphon is 84.4 m^3/s for these conditions. One of the main uncertainties in this model was the roughness of the concrete inside the barrels. Measuring this on-site instead of using textbook values could have a significant effect on the wall friction term.

The model showed that a more streamlined inlet design could increase the capacity by a maximum of 11.8 m^3/s, leading to a total of 96.2 m^3/s. This would require a curved inlet geometry rather than the current right-angled inlet, as well as a transition from the trapezoidal channel cross-section to the rectangular inverted siphon cross-section with negligible head loss. Streamlining the inlet could potentially be a simple and cost-effective way to increase the capacity of the inverted siphon, as the Juliana Canal could stay operational during construction works.

The inventory of debris accumulation showed that during winter conditions debris mostly consists of smaller branches without leaves that form floating deposits, while during summer conditions larger (non-floating) branches with leaves are more prominent. Debris as observed during July 2021 decreased the capacity of the inverted siphon to 78.0 m^3/s, a reduction of 6.4 m^3/s. This suggests that the inverted siphon capacity was indeed insufficient with respect to the Geul discharge of at least 85 m^3/s, showing that debris accumulation had a moderate but important contribution. However, the analysis was based on visual data processing of pictures taken after the event, but extensive scale model tests might give more accurate results since especially the porosity of the debris deposit was difficult to capture accurately.

It should be noted that there is little to no data available on how extreme the debris accumulation was during the July 2021 event. As such, further research to the likelihood of debris accumulation during extreme events is recommended to decide whether or not further measures are required to meet the safety standards.

An option investigated in the present project was the MEL culvert. However, data showed that a MEL culvert would not be a suitable replacement for the Geul inverted siphon, nor any other inverted siphon with a significant obstacle depth. This is because MEL culverts are designed for critical free-surface flow inside the barrel. As the barrel roof needs to be lowered so as not to obstruct the Juliana Canal (or any other obstacle), the entire barrel needs to be lowered to still allow for free-surface flow, which in turn increases the critical depth requiring even further lowering of the barrel. This leads to very narrow and high cross-section of the barrel, making it unrealistic that energy losses can be considered negligible. The conclusion is that MEL culverts quickly become unfeasible for increasing obstacle depths.

Overall this study showed that there is potential to increase the hydraulic capacity of the inverted siphon by streamlining the inlet. A more detailed cost-benefit analysis could show if streamlining the inlet could be a suitable way to meet (future) safety standards or to extend the lifetime of the inverted siphon.

Bibliography

AHN (2022). *AHN Viewer: AHN4.* From https://www.ahn.nl/ahn-viewer.

Al-Husseini, T. (2008). *Optimum Hydraulic Design of Inverted Siphon.* University of Al-Qadisiya.

Al-Juboori, M., & Al-Murshidi, K. (2021). *Optimum Hydraulic Design of Inverted Syphon Structure in Sewer System with a Case Study of Al-Hashmea Sewer Project.* KSCE Journal of Civil Engineering.

Apelt, C. (1983). *Hydraulics of Minimum Energy Culverts and Bridge Waterways.* The Instituion of Engineers, Australia.

Chanson, H. (2004). *The Hyraulics of Open Channel Flow: An Introduction (2nd edition, chapter 21).* Elsevier.

Chanson, H. (2007). *Hydraulic Performances of Minimum Energy Loss Culverts in Australia.* Journal of Performances of Constructed Facilities, ASCE, Vol. 21, No. 4, pp. 264-272 (doi:10.1061/(ASCE)0887-3828(2007)21:4(264)) (ISSN 0887-3828).

Deltares (2022). *Analyse overstromingen Geulmonding: Watersysteemevaluatie Waterschap Limburg.*

EduRev (2022). *Conveyance Structures for Canal Flows: part 3.* From https://edurev.in/studytube/Conveyance-Structures-for-Canal-Flows--Part-3--Irr/a3820863-2eb3-47e5-a644-313cbca08780_t

ENW (2021). *Hoogwater 2021: Feiten en Duiding.* Versie 2, 20 september 2021.

Gemeente Meerssen (2022). *Na het water: uitgave 7.*

Hinds, J. (1928). *The hydraulic design of flume and siphon transitions.* Transactions of the American Society of Civil Engineers.

Kirschmer, O. (1926). *Untersuchungen über den Verlust an Rechen.* Mitteilungen Hydraulisches Institut München, Nr. 1.

McKay, G.R. (1971). *Design of Minimum Energy Culverts.* Research Report, Department of Civil Engineering, University of Queensland, Brisbane, Australia.

Meusburger, H. (2002). *Energieverlusten an Einlaufrechen von Flusskraftwerken.* Technischen Hochschule Zürich.

Paarlberg, A. (1990). *Zuidlimburgse Beken en Beekdalen: Karakteristieken, Processes en Patronen.* Het Natuurhistorisch Maandblad.

Rijkswaterstaat (1927). *Technical drawing LBAN1927-8046.*

TU Delft (2022). *Water System Analysis lecture notes.*

Tullis, B. (2012). *Hydraulic Loss Coefficients for Culverts.* Utah State University.

Waterschap Limburg (2022). *Actuele waterstanden.* From https://www.waterschaplimburg.nl/uwbuurt/kaarten-meetgegevens/actuele-waterstanden/

Yaziji, H. (1968). *Open-Channel Contractions for Subcritical Flow.* Univeristy of Arizona.

Appendices

A

Technical drawings

In this appendix technical drawings of the existing inverted siphon are given. Note that dimensions and shapes in these drawings are slightly simplified compared to the real situation, to allow for analytical modelling. Data is obtained from original technical drawings (Rijkswaterstaat, 1927) and from AHN4 (AHN, 2022). Section A.1 shows the existing structure, and section A.2 illustrates what an alternative inlet could look like (explained in section 5.2).

A.1. Existing structure

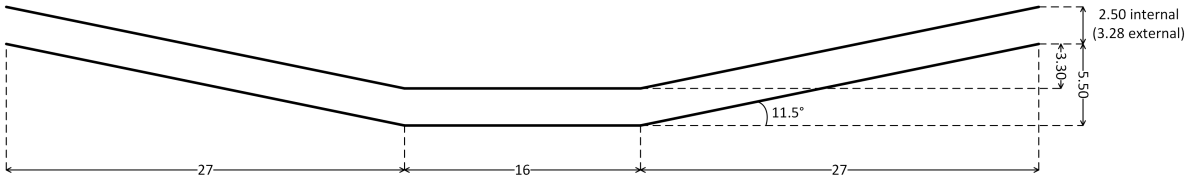

Figure A.1: Side view

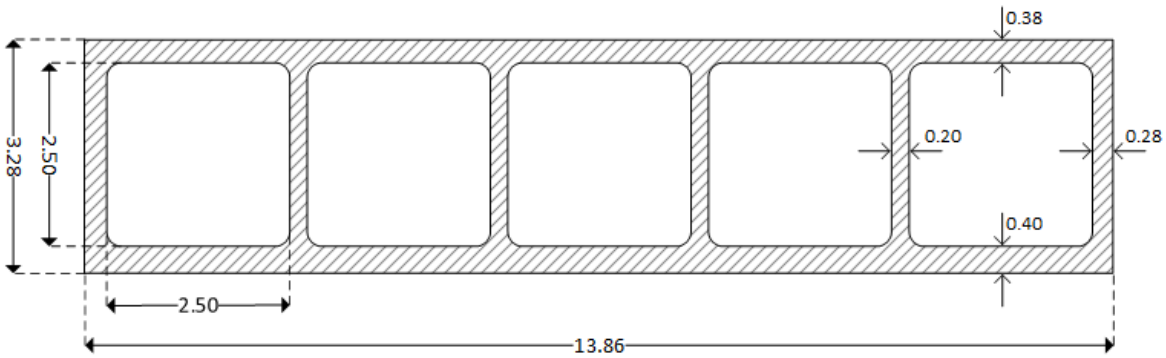

Figure A.2: Cross section

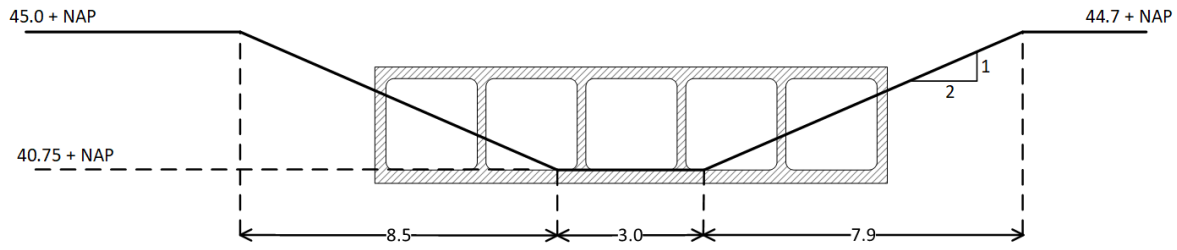

Figure A.3: Front view at cross section A-A (channel)

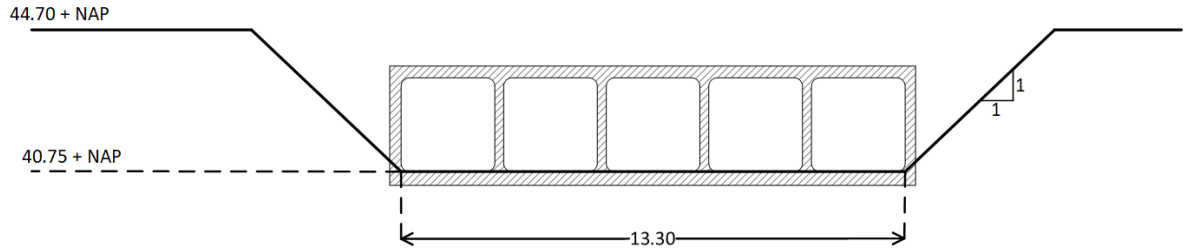

Figure A.4: Front view at cross section B-B (inlet)

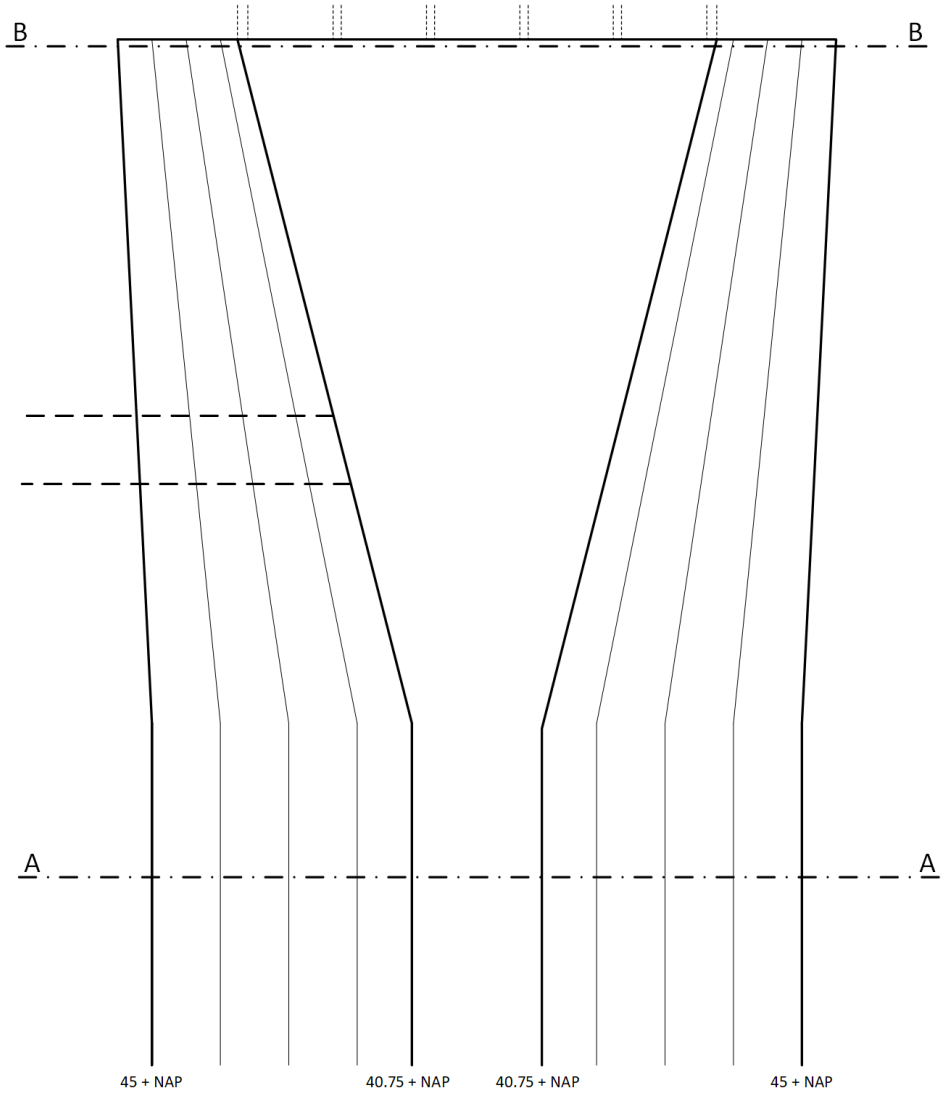

Figure A.5: Top view (upstream). The dashed lines at the left indicate the seepage stream alongside the Juliana Canal. The dashed lines at the top indicate the dividing walls of the multi-cell cross section.

A.2. Alternative (warped) inlet configuration

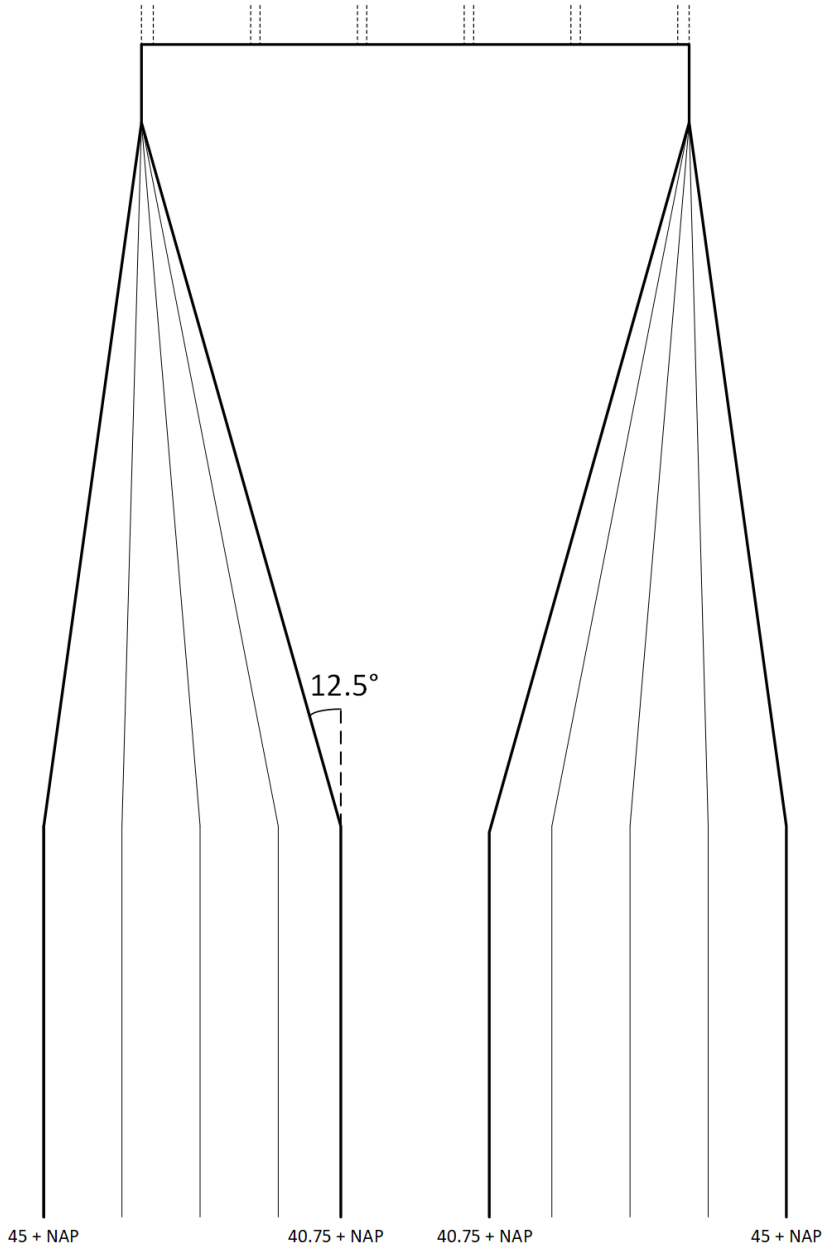

Figure A.6: Top view of an alternative inlet configuration. The dashed lines at the top indicate the dividing walls of the inverted siphon.

B

Seepage stream

This appendix gives some background on the seepage stream that connects to the Geul just before the inverted siphon inlet, and explains why it has not been included into the analysis of this report.

Along the east side of the Juliana Canal a seepage stream runs between the Beatrix Harbour and the Geul, as illustrated in figure B.2. This stream then ends up in the Geul just a couple of meters before the inverted siphon inlet, as can be seen in figure B.1 which also shows that this stream is rather shallow and not well defined. While figure B.2 shows that this stream is longer than just the reach along the Juliana Canal, it becomes even less defined the further away from the Geul it gets.

Figure B.1: Picture of the seepage stream

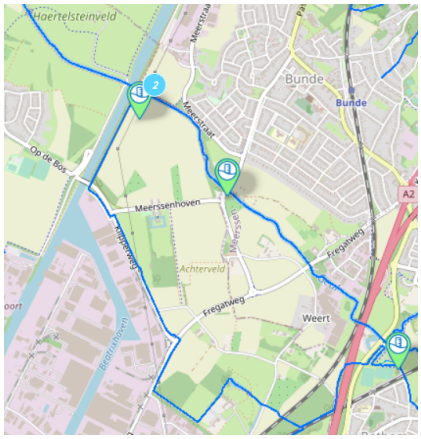

Figure B.2: Map of the seepage stream (Waterschap Limburg, 2022)

This stream is not included into the analysis of this report for two main reasons. First and foremost, there are no discharge measurements or predictions available. To obtain any reasonable discharge values an extensive hydrological model of the wider area would need to be set up. Without such a model one cannot even tell for certain in which direction the flow in this stream would be (to or away from the Geul) during extreme events similar to July 2021.

The secondary reason why this stream has not been accounted for is that there is a lack of literature on situations like these where a stream connects to a river coming from the side right before a structure inlet.

Due to the reasons mentioned above the amount of effort to model this stream appropriately is disproportionate compared to the scale of this report, especially because the conveyance capacity of this stream is small compared to the Geul and inverted siphon capacity.

C

Culvert flow patterns

This appendix gives some background on flow patterns for culverts.

Culverts can experience a range of flow patterns. Some of the main classification elements are whether the culvert is inlet controlled or outlet controlled, if there is free surface flow or pressurised flow in the barrel and if the entrance is submerged or not. If a culvert is inlet controlled then the barrel and the outlet have a larger conveyance capacity than the inlet, whereas if a culvert is outlet controlled then the inlet could take in more water than the barrel and outlet can convey. Culverts that experience pressurised flow (flowing full) are outlet controlled (Chanson, 2004).

Figure C.1 illustrates the possible flow patterns for culverts. Table C.1 gives conditions for when each flow pattern is expected to occur.

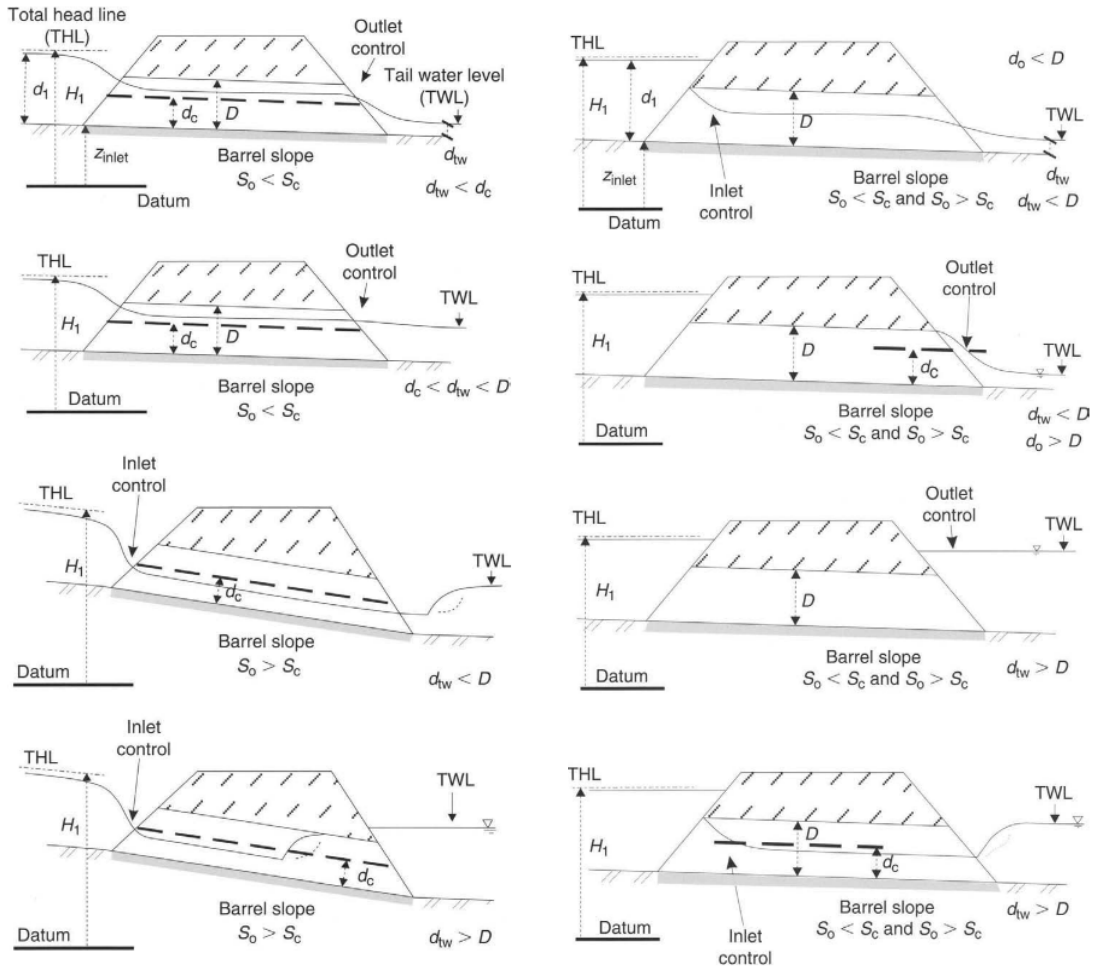

(a) free-surface inlet flow conditions

(b) submerged entrance conditions

Figure C.1: Operation of a standard culvert (Chanson, 2004). From the top to bottom case 1 to 4 are on the left, and case 5 to 8 on the right.

Flow pattern	Control location	Flow conditions	Remarks
Class I: Free-surface inlet flow			
Case 1	Outlet control	$E_0 \leq 1.2D$ $d_{tw} < d_c$ $S_0 < S_c$	
Case 2	Outlet control	$E_0 \leq 1.2D$ $d_c < d_{tw}$ and $d_{tw} > D$ $S_0 < S_c$	
Case 3	Inlet control	$E_0 \leq 1.2D$ $d_{tw} < D$ $S_0 \geq S_c$	Hydaulic jump takes place at outlet
Case 4	Inlet control	$E_0 \leq 1.2D$ $d_{tw} > D$ $S_0 \geq S_c$	Hydraulic jump takes place in barrel
Class II: Submerged entrance			
Case 5	Inlet control	$E_0 > 1.2D$ $d_{tw} < d_c$ $d_0 < D$ $S_0 < S_c$ or $S_0 > S_c$	
Case 6	Outlet control	$E_0 > 1.2D$ $d_{tw} < d_c$ $d_0 > D$ $S_0 < S_c$ or $S_0 > S_c$	Drowned barrel; critical flow depth is observed at outlet
Case 7	Outlet control	$E_0 > 1.2D$ $d_{tw} > D$ $S_0 < S_c$ or $S_0 > S_c$	Drowned barrel; usually observed for $d_0 > D$, but might occur for $d_0 < D$ if a backwater effect moves the hydraulic jump in barrel
Case 8	Inlet control	$E_0 > 1.2D$ $d_{tw} > D$ $S_0 < S_c$ or $S_0 > S_c$	Hydaulic jump takes place at outlet; usually observed for $d_0 < d_c$, may occur for $d_0 > d_c$ because of vena contracta effect at barrel intake

Table C.1: Classification of different culvert flow patterns (Chanson, 2004). Case number correspond to figure C.1.

D

Supporting theory

In this appendix a couple of equation derivations are given that are used in the main report.

D.1. Critical depth in rectangular channel

There is a relation between the specific energy and critical depth in a rectangular channel. This is based on the Bernoulli equation.

$$E = d + \frac{u^2}{2g} = d + \frac{q^2}{2gd^2}$$

For critical flow, it holds that the derivative of the specific energy with respect to the depth is equal to zero.

$$\frac{dE}{dd} = 1 - \frac{q^2}{gd^3} = 0$$

$$\frac{q^2}{g} = d_c^3$$

Combining the above expressions gives the following result.

$$E = d_c + \frac{q^2}{2gd_c^2} = d_c + \frac{d_c^3}{2d_c^2}$$

$$E = \frac{3}{2}d_c$$

D.2. Width of MEL culvert

Maximum width

Using the Bernoulli equation, an expression for the width of the channel can be derived. First the situation without invert drop is being considered. The resulting width is the maximum width B_{max} for a rectangular channel.

$$E_0 = d + \frac{u^2}{2g}$$

$$E_0 = d + \frac{Q^2}{2gB_{max}^2 d^2}$$

When critical flow is prescribed, the depth d can be replaced by the critical depth d_c, and the specific energy E_0 is equal to $\frac{3}{2}d_c$ because the channel is rectangular. See section D.1 for a derivation. The expression then becomes:

$$\frac{3}{2}d_c = d_c + \frac{Q^2}{2gB_{max}^2 d_c^2}$$

$$\frac{1}{2}d_c = \frac{Q^2}{2gB_{max}^2 d_c^2}$$

The equation can be rewritten to give an expression for B:

$$2gB_{max}^2 d_c^2 = \frac{Q^2}{\frac{1}{2}d_c}$$

$$B_{max}^2 = \frac{Q^2}{\sqrt{2g \cdot d^2 \cdot \frac{1}{2}d_c}}$$

$$B_{max} = \frac{Q}{\sqrt{g d_c^3}}$$

Or, expressed as function of the specific energy E instead of the critical depth d_c, using the results from section D.1:

$$B_{max} = \frac{Q}{\sqrt{g \cdot \left(\frac{2}{3} \cdot E\right)^3}}$$

Minimum width

The width of the MEL culvert is minimum when the invert drop is maximum. This is because a drop in elevation increases the specific energy. The specific energy E is now not constant but the initial specific energy E_0 plus the excavation depth Δz_0. Note that also this expression assumes a rectangular cross section.

$$E = E_0 + \Delta z_0$$

Using this definition for the specific energy E, the relation for B_{max} can be modified to find the relation for B_{min}.

$$B_{min} = \frac{Q}{\sqrt{g \cdot \left(\frac{2}{3} \cdot (E_0 + \Delta z_0)\right)^3}}$$

D.3. Height ratio

As explained in section 5.1 the width ratio for a horizontal contraction x_{width} is b/B, in which b is the width after the contraction and B is the width before the contraction.

$$x_{width} = \frac{b}{B}$$

However, the height ratio for the vertical contraction x_{height} at the inverted siphon entrance is a bit less straightforward. This is because the bed level remains constant (equal to the inlet opening level) and there is only a contraction at the top, unlike the horizontal contraction that narrows at both sides.

The expression below gives the height ratio as if the same contraction that happens at the top is also present at the river bed. In this D is the height of the inlet opening and d is the water depth just upstream. Note that this expression is only valid if $d > D$, otherwise there is no contraction.

$$x_{height} = \frac{D}{2 \cdot d - D}$$

Figure D.1 shows how the above expression is derived.

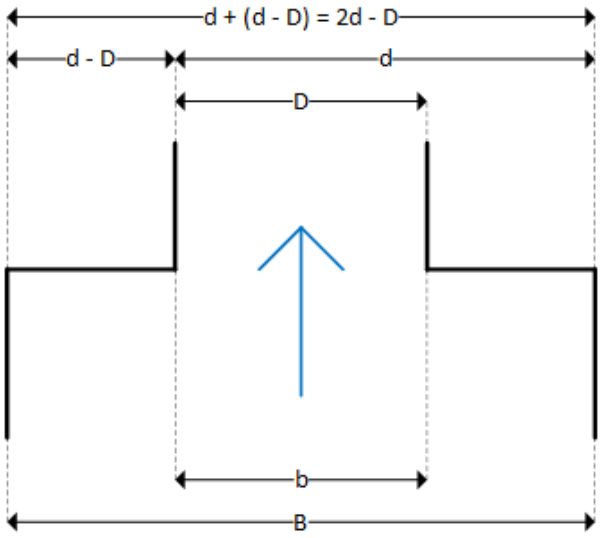

Figure D.1: Sketch supporting the definition of x_{height}

E

Pictures of debris

In this appendix a selection of pictures displaying debris at the location of interest is given. A few pictures from July 2021 have been found, but more from February 2022 when the Geul experienced high water levels again. The complete collection of pictures and videos can be requested from the author of this report.

E.1. February 2022

(a) (b)

Figure E.1: Debris deposit during February 2022 event

E.2. July 2021

(a)

(b)

Figure E.2: Close-up pictures of debris during July 2021 event

(a)

(b)

Figure E.3: Overview pictures of debris during July 2021 event

E.3. General pictures

(a) (b)

(c) (d)

Figure E.4: Branches observed, not related to a specific event